“COMPARATIVE ANALYSIS OF ATMOSPHERIC TURBULENCE-INDUCED LASER POWER FLUCTUATIONS IN A MONOLITHIC AND TILED OPTICAL RECEIVER SYSTEM”

Dual Program

Master of Science (Optics) from **Centro de Investigaciones en Óptica, A.C. (CIO)**

Master of Science in Electro-Optics from **University of Dayton (UD)**

Thesis presented by:

Marcos Enrique Valero Recio Ramírez

Advisor at CIO: Dr. Marija Strojnik

Advisor at UD: Dr. Mikhail Vorontsov

September 2020

León · Guanajuato · México

COMPARATIVE ANALYSIS OF ATMOSPHERIC TURBULENCE-INDUCED LASER POWER FLUCTUATIONS IN A MONOLITHIC AND TILED OPTICAL RECEIVER SYSTEM

Thesis

Submitted to

The School of Engineering of the

UNIVERSITY OF DAYTON

In Partial Fulfillment of the Requirements for

The Degree of

Master of Science in Electro-Optics

By

Marcos Valero

Dayton, Ohio

October 2020

ABSTRACT

COMPARATIVE ANALYSIS OF ATMOSPHERIC TURBULENCE-INDUCED LASER POWER FLUCTUATIONS IN A MONOLITHIC AND TILED OPTICAL RECEIVER SYSTEM

Name: Marcos Valero
University of Dayton

Advisors:

- Dr. Mikhail Vorontsov (University of Dayton, USA)
- Dr. Marija Strojnik (Centro de Investigaciones en Óptica A.C., México)

This research project compares the performance of a Monolithic Optical Receiver and a Multi Aperture Receiver, in order to reduce optical power fluctuations induced by a Gaussian beam traveling through atmospheric turbulence.

In this this work a mathematical model to describe the effects of focal spot wander and aperture averaging is provided, in order to explain the reduction of scintillation by increasing the area of an optical receiver. In particular, the Churnside model is used due to its simplicity to describe the effect of aperture averaging as a function of the collection diameter for receiving optical systems.

In other hand, the steps for the alignment of Multi Aperture Receiver systems are shown. In this section, interferometric tests are used to align each aperture of this optical receiver system, and thereby achieve a correct multimode fiber optic coupling of the Gaussian beam received after propagating through atmospheric turbulence. At the same time, a finder scope

is attached, which aims to align the multi aperture receiver system with the optical axis of the Gaussian beam propagated through an atospheric channel.

This work proposes a set of five experiments which use the normalized variance of the received power as a figure of merit, to compare the fluctuations of power received with both optical collectors in different conditions of atmospheric turbulence. The atmospheric channel used in practice is described in detail, and consists of a 7km optical path in the city of Dayton Ohio, which is subjected to tests in different conditions of atmospheric turbulence, that changes depending on the time of day in which measurements are done. In the case of the Multi Aperture Receiver system, it has been possible to define an effective diameter to compare the increase in sub-apertures with the increase in the total diameter of a monolithic system. With this, it has been possible to introduce a new concept called "sub-apertures averaging", referring to the classical theory of aperture averaging, applied to Multi Aperture Receiver systems.

Finally, in this work a method is proposed to find the transverse wind speed in atmospheric channels, using the cross correlation function between the power time series measured in two of the sub-apertures of the Multi Aperture Receiver system.

ACKNOWLEDGMENTS

In the first place, I would like to thank Dr. Mikhail Vorontsov for accepting me into his research group and providing me with all the necessary resources to make this project possible.

Thanks to Dr. Thomas Weyrauch for guiding me in each process of the experimental development of this thesis.

On the other hand, I am grateful for all the support of Dr. Marija Strojnik, who gave me very important advice for my academic, professional and personal training, in addition to supporting me to participate in this double degree program between the Optical Research Center (CIO) and the University of Dayton (UD).

During this two-year experience, I have had the opportunity to meet wonderful humans, both in the United States and in Mexico, who have supported me in different ways, many thanks to all of them.

To my mother and sister, from whom I have had to be away all this time, but who have supported me unconditionally.

Finally, I want to thank CONACYT, which financed my stay in the United States, trusting me and giving me a unique opportunity. I am sure that this type of program is a great opportunity for talented people who will do their best to contribute to the national development of Mexico.

TABLE OF CONTENTS

LIST OF FIGURES

LIST OF TABLES

CHAPTER I
INTRODUCTION

This first chapter shows the basic theoretical knowledge necessary to describe the fluctuations of electromagnetic waves detected by an optical receiver placed at the image plane of an arrangement which consists of a Gaussian beam propagating a determined distance through an atmospheric path which has a random temporal variation in the refractive index, also known as *atmospheric turbulence*.

In Sections 1.1 - 1.4, the composition of the atmosphere is briefly described, as well as the value of its refractive index, and how it changes due to different physical and chemical phenomena that occur in this protective layer of the earth, particularly changes in temperature and pressure. Likewise, the parameter Cn^2 is introduced to describe the statistics of the temporary fluctuations in the refractive index of the air due to temperature changes.

On the other hand, Sections 1.5 -1.10 have the purpose of deriving an analytical expression to describe in general, the intensity and phase fluctuations observed in the image plane of the optical arrangement where a Gaussian beam propagated by an atmospheric channel with different conditions of atmospheric turbulence. This can be done using the Huygens - Fresnel extended principle, solution of the Helmholtz equation, product of Maxwell's equations.

Sections 1.11 and 1.12 describes two important quantities for the analysis of power fluctuations received by different receiver optical systems used to capture the electromagnetic wavefront resulting from the propagation of a Gaussian has by atmospheric turbulence, the Fried parameter r_0 and the Rytov variance σ_I^2, with these two quantities it is possible to describe in general a series of phenomena resulting from atmospheric turbulence, such as the focal spot wander, described in Section 1.13, and the aperture averaging effect, presented in Section 1.14.

1.1. Optical properties of the atmosphere

There are factors that affect the transmission of electromagnetic radiation through the atmosphere, which are practically the same that affect our vision of distant objects (pollution, rain, snow, changes in temperature, etc.). In general, three primary effects affect the propagation of electromagnetic waves: absorption, scattering, and fluctuations in the index of refraction of the medium by which that wave travels [1]. On one side, the absorption and scattering effects are result of the chemical composition of the gases that make up the atmospheric channel , causing the attenuation of the transmitted beam; while fluctuations in the refractive index are mainly associated with temperature changes in the atmosphere, regularly due to solar radiation at different times of the day , causing the loss of spatial coherence of the electromagnetic wave, fluctuations in the irradiance of the received signal, focal spot wander for the receiving system, and other series from unwanted defects in a free-space optical communications system [2].

1.2. Composition of the atmosphere

The atmosphere is a gaseous layer that surrounds the earth and extends a few hundred kilometers over the earth's surface, its composition depends on several factors, but approximately 98% is made up of nitrogen (N_2) and oxygen (O_2) molecules , on the other hand, and in much smaller proportion, we can find in the atmosphere, molecules of some other gases like argon (Ar), neon (Ne), helium (He), krypton (Kr) and hydrogen (H_2) [3]. In addition, over the years and the accelerated industrial growth of the 21st century, the earth has seen a significant increase in so-called greenhouse gases such as water vapor (H_2O), carbon dioxide (CO_2), methane (CH_4), nitrous oxide (N_2O) and ozone(O_3) [4].

The atmosphere is usually divided into different layers at different altitudes [5], depending on the average temperature at which this layer is found. The main four layers of the atmosphere are:

- Troposphere: This is the lowest layer of the atmosphere, extends to the first 12 km above the earth's surface, and contains 75% of the atmospheric mass, and 99% of the water particles, since these are attracted to the earth by gravity. In this layer, the temperature drops rapidly with the height, reaching up to -55°C at a height of 12 km while. On the Earth's surface, the average temperature will be around 15°C, a temperature suitable for life in our planet.
- Stratosphere: In this section of the atmosphere, which typically extends from the end of the troposphere to 48 km above the earth surface, the temperature is increased to -3°C approximately, because the high concentrations of Ozone absorbs solar radiation corresponding to UV light, creating thermal energy. This layer is a shield from harmful radiation to humans.
- Mesosphere: Also called the middle layer of the atmosphere, extends from the end of the stratosphere to approximately kilometer 80 above the earth's surface. In this layer the temperature drops again to approximately -90°C, the minimum value for temperature in the atmosphere.

- Thermosphere: This layer of the atmosphere extends up to 600 km above the Earth's surface. It is called a thermosphere because the temperature increases considerably, until reaching approximately 2,000 ° C, due to the energy transfer of radiation from the sun. In this layer we can find the exosphere and the ionosphere, beginning at approximately 90 km above the earth. It is called this way because the ultraviolet light from the sun ionizes the particles in it, causing a large concentration of free electrons, and ultimately, affecting the propagation of radio waves. One of the main applications of this phenomenon is the transmission of AM radio waves.

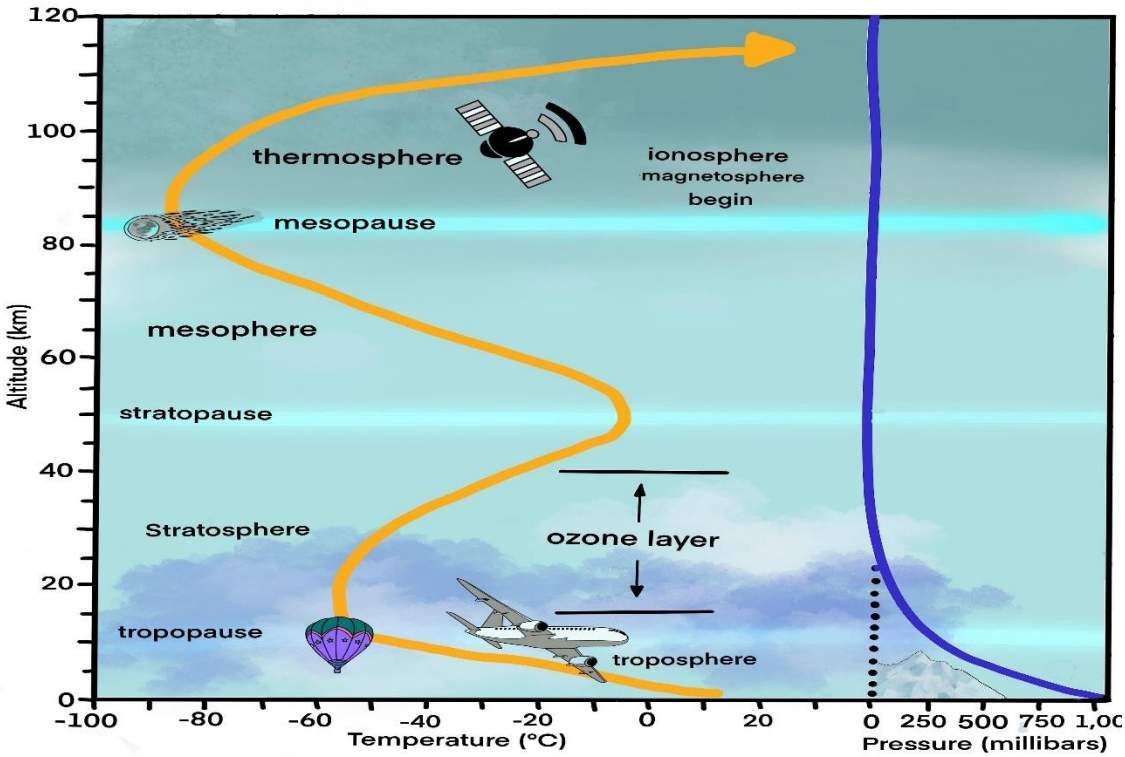

Figure 1. Temperature and pressure of the atmosphere in its different layers (US standard 1976).

Between each atmospheric layer there is a section of approximately 5 to 10 km, where the temperature remains constant, these layers are called tropopause, stratopause and mesopause. For a better visualization of the atmospheric layers see Fig. 1.

1.3. Index of refraction of the atmosphere

In general, it is possible to write to the air refractive index of the form $n = \langle n \rangle + \Delta n$, where $\langle n \rangle$ represents the average refractive index of the medium, and Δn refers to the random deviations of the average value.

There are different factors that contribute to the deformation of the wavefront to be transmitted by the atmosphere, caused by a change in the refractive index of the medium through which light propagates. Among them we can highlight the changes in temperature (in Kelvin) and pressure (in millibars) given in the air. On the other hand, such changes in the refractive index are known to have a close dependence on the wavelength (in microns) of the carrier signal. With all the above, we can find the deviation of said refractive index using the following expression [6]:

$$\Delta n = \frac{77.6 * 10^{-6} P}{T}\left(1 + \frac{7.52 \ * \ 10^{-3}}{\lambda^2}\right) \tag{1}$$

In addition to the previously mentioned quantities, we will also have a deviation in the refractive index of the atmosphere, produced by the specific humidity of that medium, this parameter contributes less than 1% in the fluctuations of the refractive index, so It will be neglected, however, there are extensive studies in which this specific humidity plays an important role when the propagation in the medium is water instead of air [7,8,9]. Under standard atmospheric conditions, at sea level, the values of the state variables in expression (1) will be: $T = 288\ K\ P = 1013\ milibars$. Generally, the wavelength used in telecommunications is 1 micrometer, resulting in a variation of the average refractive index of $\Delta n = 3 * 10^{-4}$.

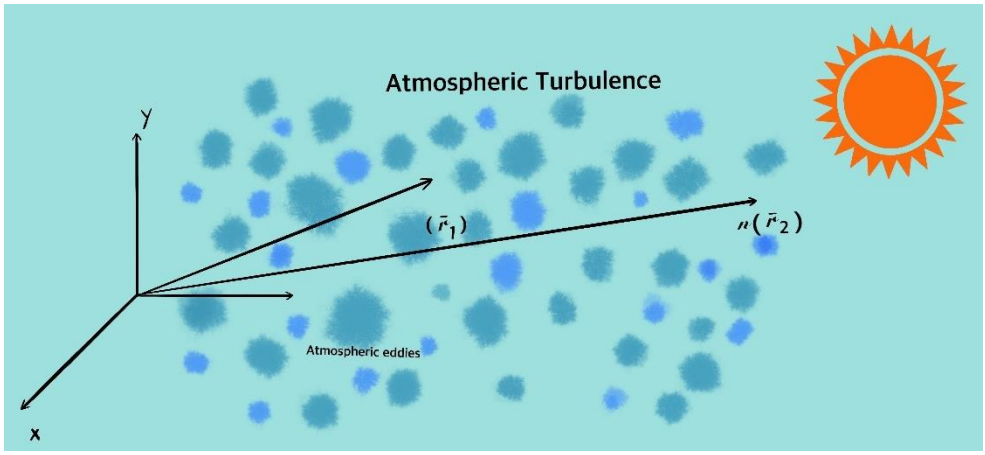

Figure 2. Vector representation of the index of refraction in different places of the atmosphere.

It is possible to represent the refractive index as a function of the position vector $\bar{\boldsymbol{r}} = \{x, y, z\} = \{\boldsymbol{r}, z\}$ and the time t, so this refractive index will take the form $n = n(\bar{\boldsymbol{r}}, t)$. To simplify the notation, *frozen times* can be considered in order to eliminate the temporal dependence in that expression for the refractive index, then $n(\bar{\boldsymbol{r}}, t) = n(\bar{\boldsymbol{r}})$. The deviations of the refractive index for a certain wavelength are caused, as mentioned above, by small changes in the fluctuation of temperature, pressure and humidity in the atmosphere, which cause eddies or *optical turbules*, of different sizes. If the optical path of the light beam to be transmitted has a relatively small length (a few kilometers), it will be maintained without major changes through large-scale eddies, larger than the aperture of the optical system. In general, these eddies will only cause a phase drift (piston phase), which is only important if the system in question is a laser interferometer, a vibrometer, Doppler lidars or communication systems based on coherent detection.

Since the fluctuations of refractive index in the atmospheric channel under study are random, the corresponding analysis must be statistical, so it is convenient to define some useful functions, for example, the covariance function:

$$B_n(\bar{\boldsymbol{r}}_1, \bar{\boldsymbol{r}}_2) = \langle n(\bar{\boldsymbol{r}}_1) n(\bar{\boldsymbol{r}}_2) \rangle \tag{2}$$

Which relates the refractive indexes at two different points in the atmospheric channel through which an electromagnetic wave propagates, we can see a vector representation of this situation, by looking at Figure 2. Homogeneities in the refractive index caused by large – scale turbules can be discriminated. The parameter associated with the maximum size of the optical turbule, known as the *turbulence outer scale* L_0, is used. Taking this particularity into account, Kolmogorov and Obukhov suggested using another statistical function, which facilitates the treatment of such deviations in the refractive index, this statistical function is called the *refractive index structure function*, defined as follows [10,11]:

$$D_n(\bar{\boldsymbol{r}}_1, \bar{\boldsymbol{r}}_2) = \langle [n(\bar{\boldsymbol{r}}_1) - n(\bar{\boldsymbol{r}}_2)]^2 \rangle \tag{3}$$

This function only depends on the homogeneities that do not exceed the distance $\rho = |\,\bar{\boldsymbol{\rho}}| = |\bar{\boldsymbol{r}}_1 - \bar{\boldsymbol{r}}_2|$. Large-scale optical inhomogeneities will not have a considerable impact on the structure function (1), but on the covariance function (2). With that said, we can infer that there is a sub-range $l_0 < \rho \ll L_0$ in the separation distance between refractive index deviations $n(\bar{\boldsymbol{r}})$, in which the random field will be uniform and isotropic. Kolmogorov and Obukhov decided to call this sub-range, as *inertial subrange*, and with it, they were able to define the *two-thirds power law*:

$$D_n(\bar{\boldsymbol{r}}_1, \bar{\boldsymbol{r}}_2) = D_n(\rho) = C_n^2 \rho^{\frac{2}{3}}, \;\; l_0 < \rho \ll L_0 \tag{4}$$

In the previous expression, we can find the constant of proportionality C_n^2, which is called *refractive index structure parameter*, and is a function of temperature, pressure, observation time, geographic location and height above ground level of the atmospheric channel through which the desired electromagnetic signals are propagated. The above model is commonly known as *Kolmogorov Turbulence*, and represents the basis of modern theory of electromagnetic wave propagation in the atmosphere.

It is complicated to define the inner l_0 and outer L_0 turbulent scales, however, the inner scale, associated with the smallest inhomogeneities in the refractive index, will have a value of a few millimeters near the ground [12]. While the outer scale, which is defined by the largest turbulence scale, is particularly difficult to define, but it is known that, for heights close to tens of meters above ground level, the relationship between these two values will be in the order of $\frac{L_0}{l_0} \approx 10^4 - 10^6$.

1.4. Refractive index structure parameter C_n^2 behavior

The refractive index structure parameter C_n^2 is present in practically all the expressions that describe the behavior of the propagation of electromagnetic waves in the atmosphere, so this is the main parameter for the description of said phenomenon. As mentioned before value of C_n^2 depends on various factors such as geographic location, observation altitude, weather conditions, and time of day, and for relatively small propagation distances (less than 10 km), this parameter is usually in the order of $C_n^2 \approx 10^{-17} - 10^{-14}\, m^{-\frac{2}{3}}$, where $10^{-17} m^{-\frac{2}{3}}$ is a weak atmospheric turbulence value, while $10^{-14} m^{-\frac{2}{3}}$, represents a strong turbulence value. As an example, we can see Figure 3, Where the time evolution of C_n^2 over a day is illustrated. These data have been taken using an atmospheric path of 7 km and practically horizontal, at a height approximate of 350 m above the sea level. It is possible to observe that the value of C_n^2 usually reaches its maximum value at some time close to solar noon, this is because the temperature rises rapidly in this time of the day. It can also be noted that the minimum value is reached at sunset and sunrise, when the temperature is homogenized, after this, the surface of the earth begins to cool and said temperature change increases the value of C_n^2.

On the other hand, the value of C_n^2 also varies depending on the height above sea level at which the observation point is located, so the structure parameter will take the form $C_n^2(h)$, this relationship is called *altitude profile*, and for this, three boundary layers are defined: the superficial boundary layer ($h \leq 1km$), the planetary boundary layer ($1km \leq h \leq 10km$), and the tropopause layer ($h > 10km$) [13]. The height of the surface boundary layer usually varies depending on atmospheric conditions.

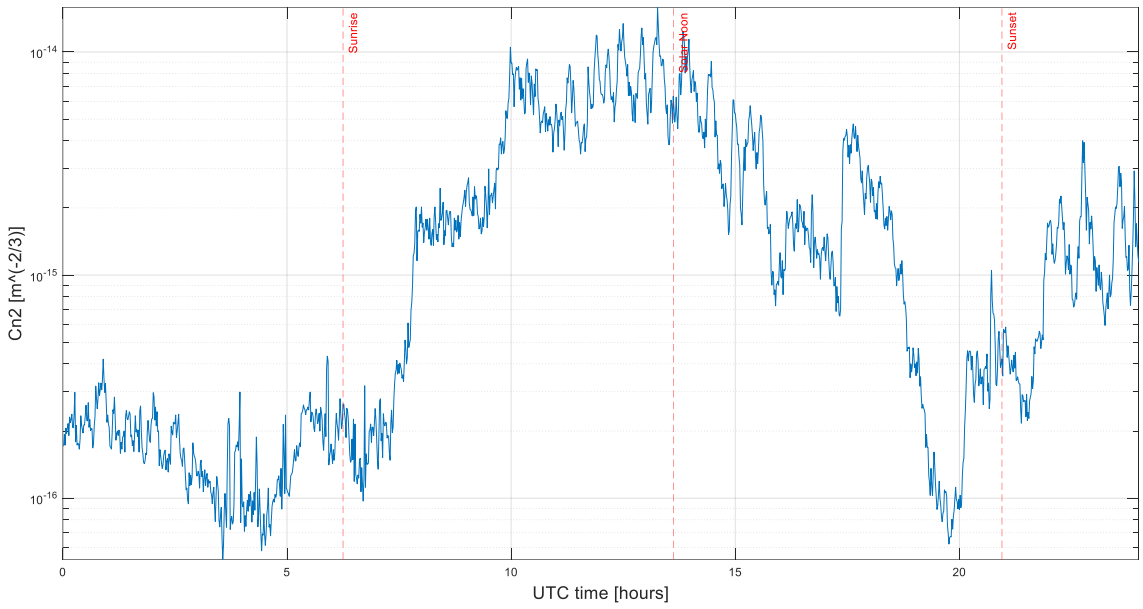

Figure 3. C_n^2 behavior throughout a day (05/20/2020), in a 7km atmospheric path located in the city of Dayton, OH.

There are some phenomenological models that describe the behavior of the structure parameter depending on the observation height [14-18]. The most common models used for this purpose for daytime conditions are the *Gracheva-Gurvich* and the *Hufnagel-Valley (HV)*. The HV model has the advantage of analytically and smoothly representing the dependency of $C_n^2(h)$, as follows:

$$C_n^2(h) = C_n^2(0)\exp\left(-\frac{h}{10^2}\right) + 5.94 * 10^{-53}\left(\frac{W}{27}\right)^2 \exp\left(-\frac{h}{10^3}\right) + 2.7 * 10^{-16}\exp\left(-\frac{h}{1500}\right) \quad (5)$$

In equation (5) there are two constants that must be adjusted, the turbulence force near the ground $C_n^2(0)$ and the wind speed at high altitudes W. The HV-21 model is commonly used, with values $W = 21\frac{m}{s}$ and $C_n^2(0) = 1.7 * 10^{-14}m^{-\frac{2}{3}}$. On the other hand, we can see that the expression (5) contains three terms

corresponding to each boundary layer. Figure 4 Shows the HV-21 turbulence profile, it is evident that the atmospheric turbulence will become weaker as the observation height increases. It is practically impossible to accurately predict the value of $C_n^2(h)$ at a height of less than 10 meters, because, at these heights, even the shape and composition of the ground contributes to the fluctuations of the air refractive index.

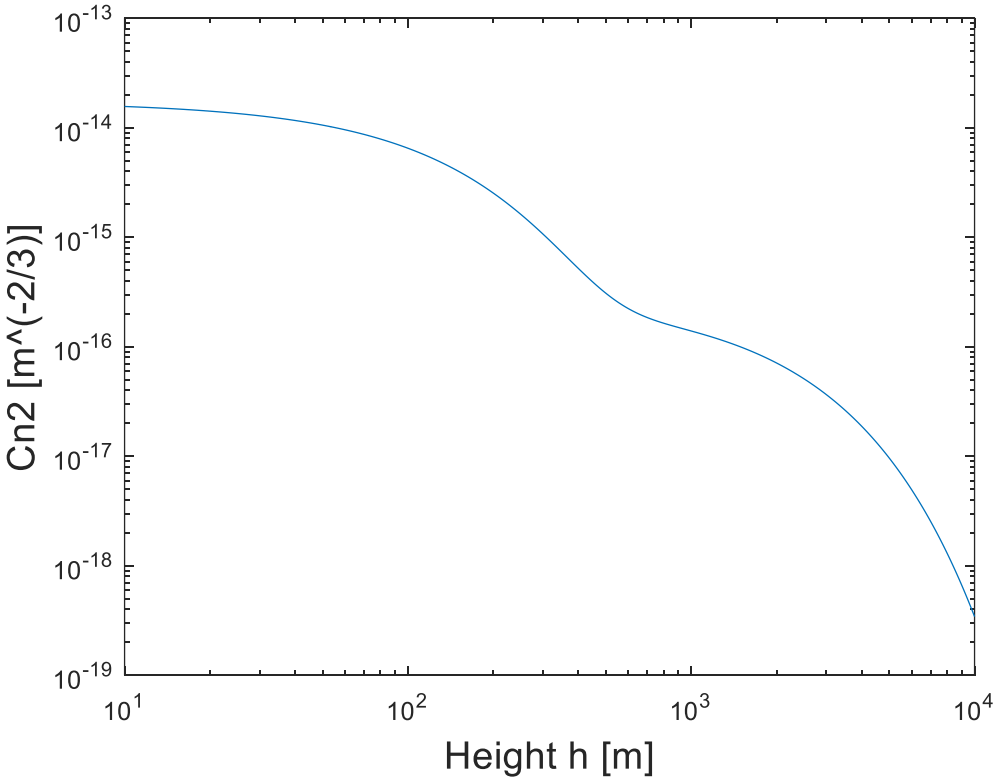

Figure 4. Model HV-21, which relates the structure parameter versus the observation height.

1.5. Atmospheric turbulence spectrum

It is possible to represent the structure function $D_n(\bar{\boldsymbol{r}}_1, \bar{\boldsymbol{r}}_2)$, in the equation (4) by means of the Fourier transform $\Phi_n(\bar{\kappa})$ of the covariance function (2), this representation is called *refractive index power spectral density function*. For isotropic and locally uniform turbulence, where the structure function only depends on the wave number $\Phi_n(\bar{\kappa}) = \Phi_n(\kappa)$ the relationship between the structure function $D_n(\rho)$ and the spectrum $\Phi_n(\kappa)$, is given by [19]:

$$D_n(\rho) = 8\pi \int_0^{\infty} \kappa^2 \, \Phi_n(\kappa) \left[1 - \frac{\sin(\kappa\rho)}{\kappa\rho}\right] d\kappa \tag{6}$$

Furthermore, we can define the *Kolmogorov turbulence spectrum*, as follows:

$$\Phi_n(\kappa) = 0.033 C_n^2 \kappa^{-\frac{11}{3}} \tag{7}$$

This expression is only valid within the borders of the spatial spectrum, corresponding to the inertial subrange, which are $k_l = \frac{2\pi}{l_0}$ and $k_L = \frac{2\pi}{L_0}$. In the general case is $k = \frac{2\pi}{l}$, where l represents the size of the turbulent eddy, so the higher the eddy is, the smaller its spectral number will be. The previous expression has a singularity at $\kappa = 0$, therefore, inspired by the Kolmogorov spectrum, some models for the refractive index power spectral density have been proposed [20], with the aim of providing a defined expression in all the spectral range $0 \leq \kappa < \infty$, as an example, is the von Karman model:

$$\Phi_n(\kappa) = 0.033 C_n^2 \exp\left(-\frac{\kappa^2}{\kappa_m^2}\right) (\kappa^2 + \kappa_L^2)^{-\frac{11}{6}} \tag{8}$$

In the previous equation $k_L = \frac{2\pi}{L_0}$ and $k_m = \frac{5.92}{l_0}$, range in which the expression (8) coincides with the Kolmogorov spectrum. There is a *jump* when the spatial wave number is close to $k_m = \frac{1}{l_0}$, for which the Andrews model [21] has been proposed, using the constants $a_1 = 1.802$ and $a_2 = 0.254$, resulting in:

$$\Phi_n(\kappa) = 0.033 C_n^2 \exp\left(-\frac{\kappa^2}{\kappa_m^2}\right)(\kappa^2 + \kappa_L^2)^{-\frac{11}{6}}\left[1 + a_1\left(\frac{\kappa}{\kappa_m}\right) - a_2\left(\frac{\kappa}{\kappa_m}\right)^{\frac{7}{6}}\right] \quad (9)$$

1.6. Free space propagation of light – Helmholtz equation

Throughout history, light has been interpreted from different points of view depending on the phenomenon that it produces, for example, if it is necessary to study the basic principles of reflection and refraction, light will be interpreted as a ray, if the purpose is to explain the photoelectric phenomenon, the light has to be interpreted as a particle (photon), and for studying the diffraction phenomenon, it is required that light be seen as an electromagnetic wave. With that fact, it is understandable that the phenomena of atmospheric optics are mostly described using the electromagnetic theory of light, because it is result of the diffraction phenomenon.

To explain the effects of atmospheric turbulence using electromagnetic theory, we take Maxwell's equations as a starting point, which describe the relationship between two vector quantities called electric and magnetic fields $\boldsymbol{E}$ and $\boldsymbol{H}$ respectively. If we assume an atmospheric path without free charges, in free space (vacuum), with permittivity ε_0, permeability μ_0 and, assuming electromagnetic fields as oscillations of the form $e^{-i\omega t}$ we can represent Maxwell's equations as follows [22]:

$$\nabla \cdot (n^2 \boldsymbol{E}) = 0$$

$$\nabla \, x \, \boldsymbol{E} = jk \sqrt{\frac{\mu_0}{\varepsilon_0}} \, \boldsymbol{H}$$

$$\nabla \cdot \boldsymbol{H} = 0 \tag{10}$$

$$\nabla \, x \, \boldsymbol{H} = -jkn^2 \sqrt{\frac{\varepsilon_0}{\mu_0}}$$

The information on the wavelength of those electromagnetic fields is contained in the wave number $k = \frac{\omega}{c} = \frac{2\pi}{\lambda}$, while the refractive index of the atmospheric channel through which it propagates will be

represented by n, in general, it will be a random function which will depend on the position of the electromagnetic wave and the physical properties of said medium,.

Despite the generality of Maxwell's equations to describe all phenomena related to electromagnetism, it is worth rewriting the behavior of electric fields traveling through the atmosphere in a more appropriate way, and only in terms of one of those fields, by convention, the electric field is chosen. This expression can be obtained in the by taking the rotational of the Faraday law:

$$\nabla \mathrm{x}(\nabla\, x\, \boldsymbol{E}) = \left(jk \sqrt{\frac{\mu_0}{\varepsilon_0}}\, \nabla \mathrm{x} \boldsymbol{H} \right) \tag{11}$$

Using the rotational properties and substituting (11) in the Gauss law:

$$\nabla(\nabla \cdot \boldsymbol{E}) - \nabla^2 \boldsymbol{E} = k^2 n^2 \boldsymbol{E} \tag{12}$$

Equation (12) is better known as the wave equation. By solving for $\nabla \cdot \boldsymbol{E}$, which we know will have a logarithmic behavior, we can obtain a final form of this equation, which will have the following form:

$$\nabla^2 \boldsymbol{E} + k^2 n^2 \boldsymbol{E} + \mathbf{2}\nabla(\boldsymbol{E} \cdot \nabla \log n) = 0 \tag{13}$$

The term $(\boldsymbol{E} \cdot \nabla \log n)$ is related to the change in the polarization of the electromagnetic wave that travels through the atmosphere, an effect studied by several authors [23-25], however, it can be neglected when the wavelength has a much lower value than the inner scale $\lambda \ll l_0$, which is generally true. It has also been shown that it is possible to avoid this term even in conditions when the wavelength is greater than the inner scale. So, the expression to analyze for behavior an electromagnetic wave propagated by the atmosphere will be:

$$\nabla^2 \boldsymbol{E} + k^2 n^2 \boldsymbol{E} = 0 \tag{14}$$

The magnetic field $\boldsymbol{H}$ will have a similar but scaled structure, in addition, the vector behavior of these fields can be ignored if it is similar in all its spatial components (x, y, z), taking only the value of the field amplitude E, and an arbitrary polarization, whereby:

$$\nabla^2 E + k^2 n^2 E = 0 \tag{15}$$

This equation, known as the *Helmholtz equation*, is the starting point in the study of an electromagnetic wave propagating in a turbulent medium.

1.7. The parabolic equation and the extended Huygens - Fresnel principle

The changes in the phase of an electromagnetic wave are caused by the imperfections and misalignments that an optical system could have, however, in this case the problem is more challenging , because those phase changes, called aberrations, are the result of wave propagation in an inhomogeneous medium with random fluctuations. To approach this problem using the Helmholtz equation (15), there is no general method for analysis, but some approximations are available. In this case, we consider the so-called *quasi-optical approximation*.

Assuming a quasi-monochromatic wave propagating in the z direction through a non-homogeneous medium, with the index of refraction $n(\bar{\boldsymbol{r}}, t)$, amplitude $A(\boldsymbol{r}, z, t)$ (also called complex envelope), and wave number $k = \frac{(n_0\omega_0)}{c}$, which is given by the refractive index in a homogeneous medium n_0. After a propagation distance $z = d$:

$$U(\bar{\boldsymbol{r}}, t) = U(\boldsymbol{r}, z, t) = A(\boldsymbol{r}, z, t)e^{-ikz} \tag{16}$$

Substituting the expression (16) into the Helmholtz equation (15). After some mathematical treatment:

$$\nabla_{\perp}^2 A + \frac{\partial^2 A}{\partial z^2} - 2ik\frac{\partial A}{\partial z} + k^2\left(\frac{n^2}{n_0^2} - 1\right)A = 0 \tag{17}$$

Where $\nabla_{\perp}^2 A = \frac{\partial^2}{\partial x^2} + \frac{\partial^2}{\partial y^2} + \frac{\partial^2}{\partial z^2}$is the transverse Laplacian operator. If the spatial scale of the refractive index inhomogeneities is much greater than the wavelength, we can assure that:

$$\left|\frac{\partial^2 A}{\partial z^2}\right| \ll k^2|A| \quad and \quad \left|\frac{\partial^2 A}{\partial z^2}\right| \ll k^2\left|\frac{\partial A}{\partial z}\right| \tag{18}$$

With the previous approximations, we can eliminate the second term from the differential equation (17), obtaining:

$$\nabla_{\perp}^2 A + k^2 \left(\frac{n^2}{n_0^2} - 1\right) A = 2ik \frac{\partial A}{\partial z} \tag{19}$$

This is known as the *parabolic equation* [26], widely used to analyze wave propagation in non-linear media, and as mentioned above, allows the study of light when the refractive index n changes due to external factors such as temperature and pressure, resulting in a variation of light intensity. We can relate the time and space dependent refractive index, with its value in a homogeneous medium, by $n(\boldsymbol{r}, z, t) = n_0 + n_1(\boldsymbol{r}, z, t)$. For atmospheric propagation, and in general for almost any application, the fluctuations in the refractive index are extremely small $n_1 \ll n_0$, whereby $n^2 - 1 \simeq 2n_1$, using this approximation:

$$\nabla_{\perp}^2 A + 2k^2 n_1 A = 2ik \frac{\partial A}{\partial z} \tag{20}$$

In the case of a traveling wave by an optically homogeneous medium:

$$\nabla_{\perp}^2 A = 2ik \frac{\partial A}{\partial z} \tag{21}$$

To solve equation (20), we use the initial condition $U(\boldsymbol{r}, z = 0, t) = A(\boldsymbol{r}, z = 0, t)e^{-ikz} = A_0(\boldsymbol{r}, t)e^{-ikz}$, obtaining the *Fresnel diffraction integral*:

$$A(\boldsymbol{r}, z, t) = \frac{ik}{2\pi z} \iint_{-\infty}^{\infty} A_0(\acute{\boldsymbol{r}}, t) \exp\left(-i \frac{k}{2z} |(\boldsymbol{r} - \acute{\boldsymbol{r}})|^2\right) d^2\acute{\boldsymbol{r}} \tag{22}$$

We can interpret this result as the superposition of different spherical waves with different amplitudes $A_0(\acute{\boldsymbol{r}})$ which emerge from a point located at $z = 0$. Interpretation that corresponds to the Huygens-Fresnel principle. It is possible to use paraxial approximation in order to replace these spherical waves with parabolic wave fronts, simplifying the corresponding analysis.

On the other hand, to describe the effect of overlapping wave fronts, caused by fluctuations in the refractive index, we can introduce an additional complex phase to the Fresnel integral (21):

$$A(\boldsymbol{r},z,t)=\frac{ik}{2\pi z}\iint_{-\infty}^{\infty}A_0(\acute{\boldsymbol{r}},t)\exp\left[-i\frac{k}{2z}|(\boldsymbol{r}-\acute{\boldsymbol{r}})|^2+\mu(\boldsymbol{r},\acute{\boldsymbol{r}},z,t)\right]d^2\acute{\boldsymbol{r}} \tag{23}$$

This representation is very useful, since it provides an expression for the complex field in the receiver, having knowledge of the complex field in the transmitter. Furthermore, it is possible to apply this principle for any turbulence regime regardless of how weak or strong it is.

In the expression (22) we can find the additional complex phase represented with the term $\mu(\boldsymbol{r},\acute{\boldsymbol{r}},z,t)=\chi(\boldsymbol{r},\acute{\boldsymbol{r}},z,t)+i\varphi(\boldsymbol{r},\acute{\boldsymbol{r}},z,t)$, expression that includes the phase $\varphi(\boldsymbol{r},\acute{\boldsymbol{r}},z,t)$ and *log-amplitude* $\chi(\boldsymbol{r},\acute{\boldsymbol{r}},z,t)$ perturbations, resulting from a spherical wave propagation from the point $(\acute{\boldsymbol{r}},z=0)$ to point $(\boldsymbol{r},z)$ by means of a non-homogeneous optical medium such as atmospheric turbulence.

Now, we can write the expression for the additional complex phase, if we take into account the relationship that exists between the phase and the amplitude of the wave at receiver $A_0(\boldsymbol{r})$, $\phi_0(\boldsymbol{r})$, with those parameters at transmitter $A(\boldsymbol{r},z,t)$, $\phi(\boldsymbol{r},z,t)$. With this:

$$\mu(\boldsymbol{r},\acute{\boldsymbol{r}},z,t)=\chi(\boldsymbol{r},\acute{\boldsymbol{r}},z,t)+i\varphi(\boldsymbol{r},\acute{\boldsymbol{r}},z,t)=\ln\frac{|A(\boldsymbol{r},z,t)|}{|A_0(\boldsymbol{r})|}+i[\phi(\boldsymbol{r},z,t)-\phi_0(\boldsymbol{r})] \tag{24}$$

The information obtained in the receiver can be encoded using amplitude and phase information, signifying an important opportunity for optical communication systems, for this reason, the coherence of the electromagnetic wave to be transmitted will play an important role, as well as the bandwidth of the traveling wave. However, it has been shown that using a partially coherent light beam can reduce the phenomena associated with atmospheric turbulence [27].

1.8. Gaussian beam in free space

In order to continue with the analysis of a traveling wave through atmospheric turbulence, it is necessary to define the type of has to propagate, in this case and generally, due to its known properties [28], a Gaussian has is used as initial wavefront, which can be expressed by the following function:

$$\psi(\boldsymbol{r}, z = 0) = \exp\left[-\left(\frac{1}{{w_0}^2.} + \frac{jk}{2R_0}\right)r^2\right] \tag{25}$$

In this representation w_0 shows the initial size of the radius of the Gaussian, also called the *Gaussian waist*, while R_0 is the initial radius of curvature of that electromagnetic wave. From this point, we will assume a flat wavefront in the transmitter, in order to facilitate future calculations, so $R_0 \to \infty$. In some literature, a solution can be found for any initial radius of curvature [29]. Considering the above, this Gaussian will have the following form:

$$\psi(\boldsymbol{r}, z = 0) = \exp - \left(\frac{r^2}{w_0^2}\right) \tag{26}$$

To know the properties of this wave after a propagation, we apply Fourier transform to (26):

$$\Psi(k_r, z = 0) = \pi w_0^2 \exp - \left(\frac{w_0 k_r}{2}\right)^2 \tag{27}$$

Where k_r represents the coordinates in Fourier space. This function will have more resemblance to a super Gaussian. Applying the spatial frequency response, the spectrum of the initial beam propagated at a distance $z = L$ from the transmitter will have the following form:

$$\Psi(k_r, z = L) = \pi w_0^2 \exp(-jk_0 z) \exp\left(-\frac{jk_r^2 q}{2k_0}\right) \tag{28}$$

The previous expression contains the *propagation constant* k_0 of the traveling wave, related with its wavelength. On the other hand, equation (28) uses the *q-parameter* of a Gaussian, defined as:

$$q = z + jz_R = z + j\frac{k_0 w_0^2}{2} \tag{29}$$

The constant $z_R$is the Rayleigh range [30]. Finally, by performing a Fourier transform to equation (29), we find the Gaussian has shape after traveling a homogeneous optical path:

$$\psi(\boldsymbol{r}, z) = \frac{w_0}{w(z)} \exp - \left(\frac{r^2}{w(z)^2}\right) \exp - \left(\frac{jk_0 r^2}{2R(z)}\right) \exp\left[-j\phi(z)\right] \exp(-j\, k_0 z) \tag{30}$$

The parameters associated with this final beam will be the following:

$$\begin{aligned} w(z) &= w_0 \sqrt{1 + \left(\frac{z}{z_R}\right)^2}, \\ R(z) &= \frac{z^2 + z_R^2}{z} \\ \phi(z) &= -\tan^{-1}\left(\frac{z}{z_R}\right) \end{aligned} \tag{31}$$

There are some references available in which the propagation of wave fronts by atmospheric channels is studied, which do not have a Gaussian profile, but rather use structured light beams. However, no significant improvement in wavefront fluctuations has been demonstrated using this type of beam [31-33].

1.9. Cumulative principle of phase aberrations

An approximate solution of equation (20) is obtained, by assuming a series of conditions that, together, are called the *geometric optics approximation*. Assuming an optical beam with radius $a_0 = w_0$. propagating a distance $z = L$, through a non-homogeneous medium, where the atmospheric eddy size is $l \ll a_0$. Then, using the normalization $\hat{L} = \frac{L}{L_{dif}} = \frac{L}{k_0}\, a_0^2 \ll 1$, the Laplacian disappears, giving the following equation:

$$2k^2 n_1 A = 2ik\frac{\partial A}{\partial z} \tag{32}$$

The solution of (32) is:

$$A(\boldsymbol{r}, z) = A_0(\boldsymbol{r}) \exp[-i\varphi(\boldsymbol{r}, z) + i\varphi_0(\boldsymbol{r})] \tag{33}$$

Where $A_0(\boldsymbol{r})$ and $\varphi_0(\boldsymbol{r})$ are the amplitude and phase of the initial wave at $z = 0$ (input plane). In the geometric optics approximation, the wave amplitude will remain unchanged $|A(\boldsymbol{r}, z)| = |A_0(\boldsymbol{r})|$, so the only effect of this propagation will be the appearance of a change in the wavefront of the form:

$$\varphi(\boldsymbol{r}, z) = -k\int_0^z n_1(\boldsymbol{r}, z')dz' \tag{34}$$

Equation (34) describes the *cumulative wavefront principle*, which provides a direct and cumulative dependence on the original wavefront with the refractive index of the linear medium by which the wave propagates a certain distance $z = L$, quantities that describe the optical path.

With all the above mathematical tools, it is possible to build an analytical model for the phase and amplitude fluctuations of a Gaussian wave propagated through atmospheric turbulence.

1.10. Phase Fluctuations

As mentioned previously, the main effect of homogeneous and isotropic atmospheric turbulence will be variations in the index of refraction of air which will produce a change in the phase of the traveling electromagnetic wave, so that each point in space will have associated a different phase of the wavefront $\varphi(\bar{\boldsymbol{r}}) = \varphi(\boldsymbol{r}, z)$. Using the covariance function (2) for the refractive index between two points $\bar{\boldsymbol{r}}_1$ and $\bar{\boldsymbol{r}}_2$, and the cumulative principle of the wavefront (34), we can find a proper covariance function for the phase change between these points:

$$B_\varphi(\bar{\boldsymbol{r}}_1, \bar{\boldsymbol{r}}_2) = \langle \varphi(\bar{\boldsymbol{r}}_1, L)\varphi(\bar{\boldsymbol{r}}_2, L)\rangle = k^2 \int_0^L dz_1 \int_0^L \langle n(\bar{\boldsymbol{r}}_1)n(\bar{\boldsymbol{r}}_2)\rangle \, dz_2 \tag{35}$$

By making the changes $r = |\bar{\boldsymbol{r}}| = |\bar{\boldsymbol{r}}_1 - \bar{\boldsymbol{r}}_2|$, $\hat{z} = z_1 - z_2$, and assuming that $B_n(\bar{\boldsymbol{r}}_1, \bar{\boldsymbol{r}}_2) = B_n\left(\sqrt{r^2 + \hat{z}^2}\right)$, the equation (35) is going to take the form:

$$B_\varphi(\bar{\boldsymbol{r}}_1, \bar{\boldsymbol{r}}_2) = k^2 \iint_0^L B_n\left(\sqrt{r^2 + \hat{z}^2}\right) dz_1 dz_2 \tag{36}$$

If the propagation distance meets the condition $L \gg \hat{z} \sim l_n$, we can extend the integration limits to infinity, thus:

$$B_\varphi(r, L) = k^2 \int_0^\infty B_n\left(\sqrt{r^2 + \hat{z}^2}\right) d\hat{z} \tag{37}$$

Substituting the spectrum $\Phi_n(\kappa)$, like in the expression (6), and using the integral representation of the zero-order Bessel function $J_0(\kappa r)$ the expression (37) can be transformed into:

$$B_\varphi(r, L) = 4\pi^2 k^2 L \int_0^\infty \Phi_n(\kappa) J_0(\kappa r) \kappa d\kappa \tag{38}$$

At $r = 0$, we can find the *phase fluctuation variance* $\sigma_\varphi^2 = B_\varphi(0, L)$, an important property to characterize the phase fluctuations due to atmospheric turbulence. With this:

$$\sigma_\varphi^2 = 4\pi^2 k^2 L \int_0^\infty \Phi_n(\kappa)\, \kappa d\kappa \tag{39}$$

On the other hand, we can express this variance of phase fluctuations using the statistical function of Kolmogorov and Obukhov $D_\varphi(r, L)$, in terms of the previously mentioned covariance function $B_\varphi(r, L)$, as follows:

$$D_\varphi(r, L) = 2[B_\varphi(0, L) - B_\varphi(r, L)] = 2[\sigma_\varphi^2 - B_\varphi(r, L)] \tag{40}$$

Using the above property and the equation (38):

$$D_\varphi(r, L) = 4\pi^2 k^2 L \int_0^\infty 2\kappa * \Phi_n(\kappa)\, [1 - J_0(\kappa r)] d\kappa \tag{41}$$

In the previous integral the spatial filtering $F(\kappa, r) = 2\kappa[1 - J_0(\kappa r)]$ corresponding to the geometric optics approach [34] is included, with this filter, it is possible to define the contribution of each spectral component of fluctuations of refractive index at each point r.

It is possible to use the *Rytov approximation* [35] which considers more complex diffraction effects, by using the help of the following spatial filtering:

$$F(\kappa, r) = \kappa[1 - J_0(\kappa r)] \left[1 + \frac{\sin\left[\left(\frac{k}{k_F} \right)^2 \right]}{\left(\frac{k}{k_F} \right)^2} \right] \tag{42}$$

$k_F = \sqrt{\frac{k}{L}} = \sqrt{\frac{2\pi}{\lambda L}} = \frac{\sqrt{2\pi}}{r_F}$ corresponds to the inhomogeneities of the refractive index corresponding to the radius of the Fresnel zone zero r_F. This approximation has no impact on the large-scale spectral components of the refractive index fluctuations with a value of $\kappa < k_F$, therefore, the expression (41) will be more than

enough under this condition. On the other side, the homogeneity components of the small-scale refractive index $l_n \ll r_F$ will have a significant impact depending on the structure of the fluctuations.

It is very useful to consider the following functions, which relate the characteristics of phase fluctuations σ_φ^2 and the statistical function $D_\varphi(r, L)$ with their corresponding phase, this is possible by assuming a Gaussian probability distribution and statistically stationary, homogeneous and isotropic fluctuations in the refractive index:

$$\langle e\text{^}i[\varphi(r,L)]] \ \rangle = e\text{^}(-((\sigma\_\varphi\text{^}2)/2)\ ) \tag{43}$$

$$\left\langle e^{i[\varphi(\boldsymbol{r_1},L)-\varphi(\boldsymbol{r_2},L)]} \right\rangle = e^{-\left(\frac{D_\varphi(r,L)}{2}\right)} \tag{44}$$

It is possible to substitute the different models for the spectral power density function of the refractive index $\Phi_n(\kappa)$ in equation (38). however, the Kolmogorov model (7) does not consider values outside the inertial sub-range, reason why the most appropriate model in this case is the von Karman model (8), with this, by solving the integral, the variance of the phase fluctuations will be:

$$\sigma_\varphi^2 = 0.4 C_n^2 \kappa^2 L L_0^{\frac{5}{3}} \tag{45}$$

Equation (45) contains the turbulence outer scale L_0 , which is very complicated to determine experimentally, so the analysis of phase fluctuations using this approximation is not easy either. If $l_0 \ll r$, we can numerically solve the integral (41), using the Kolmogorov (7) spectrum, whereby the phase fluctuation structure function, under the regime of the geometric approximation, will have the form:

$$D_\varphi(r, L) = 2.92 C_n^2 \kappa^2 L r^{\frac{5}{3}} \tag{46}$$

1.11. The receiver coherence diameter - Fried Parameter

It is possible express the (46) function using the following expression:

$$D_{\varphi}(r) = D_{\varphi}(r, L) = \left(\frac{r}{r_c}\right)^{\frac{5}{3}} \tag{47}$$

Expression in which the *phase fluctuation correlation distance* r_c is introduced, and has the following structure:

$$r_c = (2.92 C_n^2 \kappa^2 L)^{-\frac{3}{5}} \tag{48}$$

In any case, the most popular way of representing the phase fluctuation structure function is as follows:

$$D_{\varphi}(r) = D_{\varphi}(r, L) = 6.88 \left(\frac{r}{r_0}\right)^{\frac{5}{3}} \tag{49}$$

The *receiver coherence diameter* r_0 is defined, a parameter introduced by Fried in 1966 [36], which is why it is now known as the *Fried parameter*:

$$r_0 = 1.68 (C_n^2 \kappa^2 L)^{-\frac{3}{5}} \tag{50}$$

It is convenient to use the expressions (48) and (50) because the phase fluctuations will have a constant value, depending on the value of the parameter C_n^2, if it exists. C_n^2 can be easily measured in the laboratory, making the theoretical-experimental process much easier when using these parameters.

The $\frac{D}{r_0}$ ratio is commonly used to characterize the effect of atmospheric turbulence in different optical systems.

1.12. Scintillation Index and the Rytov approximation

As mentioned in Section 1.7, the Fresnel integral (22), which provides an approximate expression for the electromagnetic wave in the receiver after traveling through an atmospheric channel, includes a phase change which has been briefly studied. However, expression (23) also includes a change in the log-normal amplitude, which will allow statistical analysis of the amplitude fluctuations that occur in a receptor. Similar to equation (41), using the Rytov approximation, we will have for the amplitude fluctuations:

$$D_\chi(r,L) = \langle[\chi(\bar{\boldsymbol{r}}_1,L) - \chi(\bar{\boldsymbol{r}}_2,L)]^2\rangle = 4\pi^2 k^2 L \int_0^\infty \Phi_n(\kappa) F(\kappa,r) d\kappa \tag{51}$$

$\chi(r,L)$ is the log-amplitude defined in equation (24), however, in this case the spatial filtering function has the form:

$$F(\kappa,r) = \kappa[1 - J_0(\kappa r)]\left[1 - \frac{\sin\left[\left(\frac{k}{k_F}\right)^2\right]}{\left(\frac{k}{k_F}\right)^2}\right] \tag{52}$$

At first glance it might seem that this expression only differs from the spatial filtering function (42) by a sign, however this has a deeper implication, emphasizing mostly the spectral components of fluctuations of the small-scale refractive index $\kappa > k_F$. This means that the large-scale components in the refractive index will have no impact on the function $D_\chi(r,L)$. Another similarity with the phase fluctuation expressions is the possibility to use equations (43) and (44) and adapt them to our variable of interest, obtaining:

$$\langle e^{i[\varphi(r,L)]]}\rangle = e^{-\left(\frac{\sigma_\varphi^2}{2}\right)} \tag{53}$$

$$\left\langle e^{i[\chi(\boldsymbol{r_1},L) - \chi(\boldsymbol{r_2},L)]}\right\rangle = e^{-\left(\frac{D_\chi(r,L)}{2}\right)} \tag{54}$$

σ_χ^2 is called *log-amplitude variance* and it can be defined using the Rytov approximation by the following expression [37]:

$$\sigma_\chi^2 = \langle \chi^2 \rangle = 0.31 \kappa^{\frac{7}{6}} C_n^2 L^{\frac{11}{6}} \tag{55}$$

Expression (55) is used to estimate the amplitude and intensity of the fluctuations (scintillation), in a range known as the *weak fluctuation regime* condition that is satisfied when the variation of amplitude takes the values of $\sigma_\chi^2 < 0.25$, however, has been demonstrated that this approximation can be used even when $\sigma_\chi^2 \simeq 1$, or even higher values. This shows that the dependence on phase and amplitude fluctuations is weak, and it shows as well that the approximation of amplitude fluctuations is more tolerant to strong turbulence values than the phase fluctuations does.

Another important statistical quantity is the well-known *scintillation index*, which relates the variations in intensity (scintillations) received after a certain L propagation through an atmospheric channel:

$$\sigma_I^2 = \frac{\langle (I - \langle I \rangle)^2 \rangle}{\langle I \rangle^2} = \frac{\langle I^2 \rangle}{\langle I \rangle^2} - 1 \tag{56}$$

Where $I \equiv I(\boldsymbol{r}, L) = |A(\boldsymbol{r}, L)|^2$. It can be shown that, under weak fluctuation conditions, the scintillation index can be approximated using the *Rytov variance* [38], another important quantity in the analysis of fluctuations of an electromagnetic wave propagating through an atmospheric channel, because like the Fried parameter, it can also be represented using a constant value with the following expression:

$$\sigma_I^2 = e^{\sigma_R^2} - 1 \simeq \sigma_R^2 = 4\sigma_\chi^2 \tag{57}$$

So finally, the Rytov variance can be approximated by a constant representation of the form:

$$\sigma_R^2 = \sigma_1^2 = 1.23 C_n^2 \kappa^{\frac{7}{6}} L^{\frac{11}{6}} \tag{58}$$

All the above parameters are easily known in any experimental setup, particularly in the University of Dayton at the intelligent optics laboratory, where we use a laser with a Gaussian profile of $\lambda = 1.062\mu m$, propagating at a distance of $L = 7{,}000m$.

Using those conditions, we can plot the graph shown in Figure 5. In this graph it can be seen that, with those particular characteristics, the conditions of weak fluctuations $\sigma_1^2 < 1$ will only be reached when the parameter $C_n^2 < 10^{-15}\left[m^{-\frac{2}{3}}\right]$, however, taking into account that the fluctuations of log-normal amplitude can take values of up to σ_1 ^ 2≃4 or more, it can be thought that said approximation may be valid up to values close to $C_n^2 < 10^{-14}\left[m^{-\frac{2}{3}}\right]$. In the Figure 3 It can be seen that, for a normal day in the city of Dayton, using a 7,000m atmospheric channel, the values of the structure parameter will be in a range of $10^{-16} < C_n^2 < 10^{-14}$. With this, we can see that the previous model is a little tight but enough in the analysis of power fluctuations in the optical receive system.

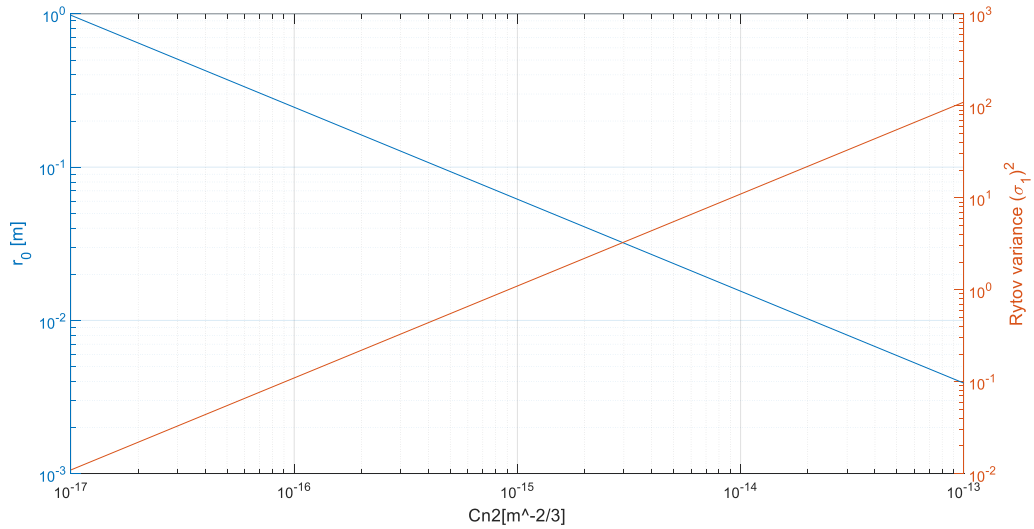

Figure 5. Relationship between the parameters r_0 and σ_1^2 with different values of C_n^2, for the propagation of a Gaussian has of $\lambda = 1.062\mu m$, through an atmospheric channel of $L = 7\ km$.

1.13. Variance of arrival angle and focal spot wander

One of the main effects of phase fluctuations (39), is the change in the angle of incidence α of the light beam at the receiver, after propagating through the atmospheric channel of interest, which will produce a displacement r_F of the focal spot after that electromagnetic wave is intercepted by the objective, which can be represented by a lens. This is of vital importance when looking to couple the received power to an optical fiber whose relatively small core size, a situation that frequently occurs in single-mode fibers. In this situation, the variation in the focal spot will produce an extra fluctuation in the received power, independent of the fluctuation in the receiver optical system.

On the other side, if the goal is to avoid the optical fibers, using a sensor with a relatively large size, the variation in the focal spot will not represent a technical challenge and the variations in power received in that sensor will be the same as in the receiver.

It is important to mention that the following analysis is only defined in the regime of weak fluctuations, and this will be strictly, because as mentioned previously, the displacement of the focal spot is a product of phase fluctuations, and unlike fluctuations in amplitude, these phase fluctuations do not allow much room to analyze strong fluctuations.

Let's consider a plane wave propagating in atmospheric turbulence at a distance L, entering a receiving lens defined by a diameter D and a focal length F. Due to the phase fluctuations in said electromagnetic wave, the wavefront will suffer random fluctuations in its arrival angle, which can be estimated as $\alpha = \frac{\Delta\varphi}{kD}$, where $\Delta\varphi$ is the phase difference at a distance D. With the above, we can find the fluctuation of the radial distance of the focal spot $r_F = F\alpha = \frac{F\Delta\varphi}{kD}$. Therefore, the average of the magnitude of the focal spot wander can be obtained using the following expression:

$$\sigma_F = \sqrt{\langle {r_F}^2 \rangle} = F\sigma_\alpha = \frac{F\sqrt{\langle \Delta\varphi^2 \rangle}}{kD} \tag{59}$$

In the previous expression σ_α is the standard deviation of the angle of arrival. On the other hand, we can determinate the phase change given by $\langle \Delta\varphi^2 \rangle = D_\varphi(r = D)$. By using equation (59), we obtain:

$$\sigma_\alpha^2 = \frac{6.88\left(\frac{D}{r_0}\right)^{\frac{5}{6}} F}{kD} = \frac{0.174\left(\frac{D}{r_0}\right)^{\frac{5}{6}} F\lambda}{D} \tag{60}$$

At the same time, for the standard deviation of the focal spot wander:

$$\sigma_F = \frac{2.6\left(\frac{D}{r_0}\right)^{\frac{5}{6}} F}{kD} = \frac{0.42\left(\frac{D}{r_0}\right)^{\frac{5}{6}} F\lambda}{D} \tag{61}$$

A more suitable approach, which contemplates phase fluctuations at various spatial scales, is given by [15]:

$$\sigma_F = \begin{cases} \simeq \dfrac{3.6\left(\frac{D}{r_0}\right)^{\frac{5}{6}} F}{kD} \; for\; L < 0.25D^2\kappa \\ \simeq \dfrac{2.6\left(\frac{D}{r_0}\right)^{\frac{5}{6}} F}{kD} for L > D^2\kappa \end{cases} \tag{62}$$

1.14. Aperture averaging

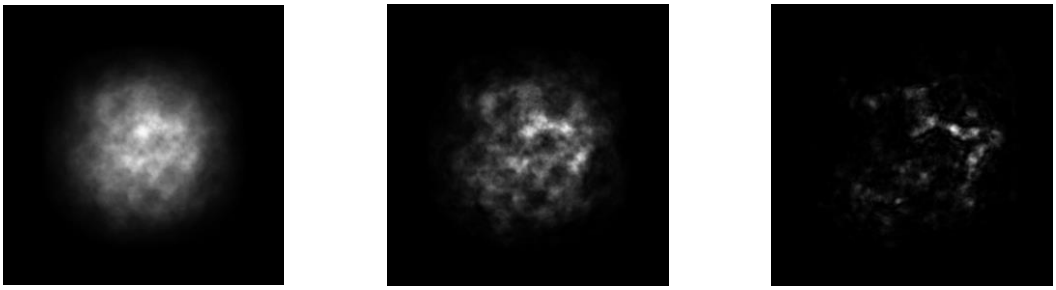

(a) (b) (c)

Figure 6. $1m^2$ screen showing a $\lambda = 1.064\ \mu m$ Gaussian beam with an initial diameter of $D_0 = 2.5\ cm$ after a propagation distance of $L = 7\ km$ by atmospheric turbulence with a) $C_n^2 = 1e-16\ m^{-\frac{2}{3}}$, b) $C_n^2 = 1e-15\ m^{-\frac{2}{3}}$, c) $C_n^2 = 1e-14\ m^{-\frac{2}{3}}$ (10 iterations).

Fluctuations in amplitude and phase of laser light due to propagation through atmospheric turbulence significantly affect the quality and shape of the electromagnetic signal in the receiver, creating regions of the beam footprint where the intensity is considerably decreased (fading regions), and at the same time regions in which that intensity will be higher than expected (hot spots). This can be clearly observed in Figure 6, in which the simulation of the propagation of a $\lambda = 1.064\ \mu m$ Gaussian has is performed, with an initial diameter of $D_0 = 2.5\ cm$ through an atmospheric channel of $L = 7\ km$, at an altitude of $h = 300\ m$, with different values of C_n^2. It can be seen that, because of atmospheric turbulence, the beam decomposes as the factor C_n^2 increases.

One of the ways to quantify the quality of the received information after light propagates in the free space is through power measurements at the receiver, particularly a circular telescope with diameter D. This received power is also often referred to as *power in the bucket*, and will generally be of the form $P = \int I(\boldsymbol{r}, L)$, where, as previously mentioned, L is the propagation distance of the beam, $\boldsymbol{r}$ is a transverse vector and $I(\boldsymbol{r}, L)$ is the irradiance in the plane of the collector lens. In the case of a plane or spherical wave, this is given by [18]:

$$\langle P \rangle = \frac{1}{8}\pi D^2 \langle I \rangle, \quad [W] \tag{63}$$

Due to the scintillation phenomenon this power will not remain constant over time and, on the contrary, will be randomly changing depending on the turbulence conditions. Since the 1950s it was demonstrated by means of astronomical measurements that power fluctuations due to scintillation decreased with increasing collection area of the telescope at the receiver [39], this is known as "averaging aperture", and more recently , this concept has been used for free space laser communication applications [1, 40-41].

The most widely used statistical quantity to describe the power fluctuations in the collector is the normalized variance, the expression of which is as follows:

$$\sigma_P^2(D) = \frac{\langle P^2 \rangle - \langle P \rangle^2}{\langle P \rangle^2} \tag{64}$$

The previous quantity is usually called as "aperture averaging factor" A, which can be expressed by means of the integral proposed by Tatarskii [34]:

$$\sigma_P^2(D) = A = \frac{16}{\pi D^2}\int_0^D b_I(\rho)\left[\cos^{-1}\left(\frac{\rho}{D}\right) - \frac{\rho}{D}\left(1 - \frac{\rho^2}{D^2}\right)^{\frac{1}{2}}\right]\rho d\rho \tag{65}$$

In the previous expression $b_I(\rho) = \frac{B_I(\rho)}{B_I(0)}$ is the normalized covariance of the irradiance fluctuations, in addition to the fact that the quantity in parentheses refers to the optical transfer function, proportional to the area of olverlap of two circles of diameter D, separated by a distance ρ.

Another common representation of the aperture averaging factor is given by:

$$A = \frac{\sigma_I^2(D)}{\sigma_I^2(0)} \tag{66}$$

Where the scintillation index for an opening with diameter D is related to the scintillation index for a point aperture $D = 0$.

It is important to note that factor A is not a statistical quantity that directly describes atmospheric turbulence-induced fluctuations, but rather, describes the reduction of intensity scintillation, in the log intensity variance $\sigma_{\ln I}^2$ for a non -point receiver.

The exact analytical expressions for the aperture averaging factor are limited because it is very difficult to determine an expression for the spatial covariance function $B_I(0)$. Therefore, to attack this problem, researchers on the subject have been forced to use numerical approximations for different cases with atmospheric conditions [40-43]. Particularly, there are very elegant approaches for the case of the fluctuations on the weak atmospheric regime, however, to study the strong turbulence regime, the expressions are complicated and give rise to quite complicated polynomials.

Since the objective of this work is not to carry out the complicated mathematical developments to find the appropriate expressions of the aperture averaging factor, but rather, to use the existing theory to compare it with the experimental data, we will summarize the results of the work of James H. Churnside [44], in Table 1. In which the approximate analytical expressions are shown to find the aperture averaging factor under different conditions of atmospheric turbulence. We will assume that the traveling wave does not significantly change its radius of curvature, therefore, it can be considered as a plane wave.

It is important to note that in expressions (67) and (69) the approximation for the averaging factor A considers that the smallest turbulent eddy size (inner scale) in this atmospheric channel is $l_0 = 0$, so these expressions do not consider this term.

Table 1. Aperture averaging expression for different atmospheric turbulence conditions.

	Condition	Formula	
Weak turbulence	$r_0 \geq \left(\frac{L}{k}\right)^{\frac{1}{2}}$ $l_0 \leq 2.73\left(\frac{L}{k}\right)^{\frac{1}{2}}$	$A = \left[1 + 1.07\left(\frac{kD^2}{4L}\right)^{\frac{7}{6}}\right]^{-1}$	(67)
	$r_0 \geq \left(\frac{L}{k}\right)^{\frac{1}{2}}$ $l_0 > 2.73\left(\frac{L}{k}\right)^{\frac{1}{2}}$	$A = \left[1 + 2.21\left(\frac{D}{l_0}\right)^{\frac{7}{3}}\right]^{-1}$	(68)
Strong turbulence	$r_0 < \left(\frac{L}{k}\right)^{\frac{1}{2}}$ $l_0 \leq r_0$	$A = \frac{\sigma_I^2 + 1}{2\sigma_I^2}\left[1 + 0.908\left(\frac{D}{2\rho_0}\right)^2\right]^{-1} + \frac{\sigma_I^2 - 1}{2\sigma_I^2}\left[1 + 0.162\left(\frac{k\rho_0 D}{2L}\right)^{\frac{7}{3}}\right]^{-1}$ $\rho_0 = (1.46k^2 LC_n^2)^{-\frac{3}{5}}$ $\sigma_I^2 = 1 + 1.22\left(\frac{k{\rho_0}^2}{L}\right)^{\frac{1}{3}}$	(69)
	$r_0 < \left(\frac{L}{k}\right)^{\frac{1}{2}}$ $l_0 > r_0$	$A = \frac{\sigma_I^2 + 1}{2\sigma_I^2}\left[1 + \left(\frac{D}{2\rho_0}\right)^2\right]^{-1} + \frac{\sigma_I^2 - 1}{2\sigma_I^2}\left[1 + 1.27\left(\frac{k\rho_0 D}{2L}\right)^{\frac{7}{3}}\right]^{-1}$ $\rho_0 = \left(1.20k^2 LC_n^2 l_0^{-\frac{1}{3}}\right)^{-\frac{3}{5}}$ $\sigma_I^2 = 1 + 1.21\left(\frac{k\rho_0 l_0}{L}\right)^{\frac{1}{3}}$	(70)

CHAPTER II
EXPERIMENTAL ARRANGEMENT TO STUDY POWER FLUCTUATIONS IN A MONOLITHIC AND TILED RECIEVER OPTICAL SYSTEM

This chapter describes the electro-optical arrangement used for the experimental comparison of a monolithic receiver and a multi-aperture receiver that collect optical power fluctuations caused by propagation of a Gaussian beam through atmospheric turbulence.

Section 2.1 describes the experimental arrangement with which optical atmospheric turbulence tests are performed in the Intelligent Optics Laboratory at the University of Dayton, consisting of an optical path of ~ 7 km with random fluctuations in its index of refraction due to real atmospheric turbulence conditions. In the image plane of this arrangement (beacon platform), there is a semiconductor laser system that creates a Gaussian beam of $d = 2.5\ cm$ and $\lambda = 1.06\ \mu m$, in Section 2.2 the components of this beacon platform are described.

On the other hand, in the image plane of this 7 km optical arrangement, there are a series of optical receivers that are mentioned in Section 2.3, while in the following sections a more in-depth analysis of the components that make up the pair of receptors to be compared in this experimental work, a monolithic receptor system (Section 2.4) and a multiple-aperture system (Section 2.5). Particularly for the multiple aperture system, it is necessary to carry out a very specific assembly and alignment, in order to avoid blurring and / or tilts in each of the lenses of its apertures, which is why a section is dedicated to describe this process (Section 2.6), where the different optical tests performed on this instrument are described. Finally, once the optical receivers have been properly aligned and placed in the image plane of this optical arrangement, it is necessary to have a data acquisition and processing system to obtain useful information on the power variations received with the instruments. Opticians mentioned above, to explain the details of this data acquisition, Section 2.7 of this work is included.

2.1. Atmospheric testbed (7 km)

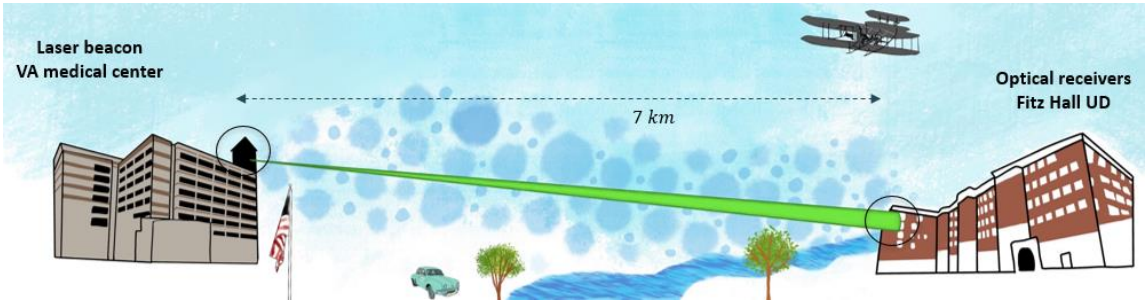

Figure 7. Atmospheric testbed for atmospheric optics at the university of Dayton.

All the experimental activities in this work were carried out in the atmospheric testbed at the University of Dayton. The UD target-in-the-loop atmospheric sensing testbed and sensing system provide capabilities for direct evaluation of the impact of various atmospheric effects on laser beam characteristics. This research utilizes the $L = 7\ km$ unidirectional atmospheric propagation path that links the beacon platform located on the roof of the Dayton VA Medical Center (VAMC) and the sensing modules positioned on the 5th floor of the UD College Park Center building, this is illustrated in Figure 7.

It is possible to control the transmitter remotely from the receiver, and at the same time, the testbed at the University of Dayton has a scintillometer that is updated every minute and gives the value of C_n^2 in real time for the corresponding arrangement, with this, the measurements taken using different optical receiver systems, can be compared with the value given by that instrument. On the other hand, this testbed has a couple of weather stations, one in the transmitter and another one in the receiver, so if necessary, information can also be obtained in real time for the wind speed and the air temperature.

2.2. Beacon platform characteristics

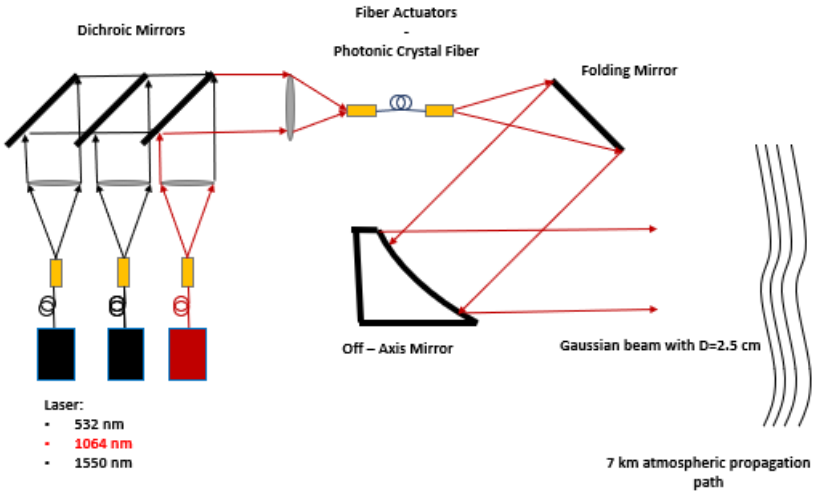

Figure 8. Schematic diagram of the laser transmitter for the atmospheric testbed at the intelligent optics laboratory.

The initial Gaussian beam to be transmitted through the atmospheric is produced by a laser source located on the roof of the VA medical center building in the city of Dayton, in that building there is a special cabin on the top, in which is a small laboratory dedicated to producing a Gaussian beam of $D_0 = 2.5\ cm$, at different wavelengths ($\lambda = 0.532\ \mu m, 1.064\ \mu m, 1.554\ \mu m,$), in order to do this, the configuration shown in Figure 8 is used. As can be seen, three lasers with their respective current and temperature regulators are coupled by means of a lens to a photonic crystal fiber, which combine these beams without losing information or introducing aberrations. Each laser has an actuator which can maximize the power delivered with the help of a controller software, at the same time, the photonic crystal fiber has another actuator that will be used to direct the beam with small changes in the shooting angle.

After light propagates through the fiber combiner, a folding mirror with the help of an off axes parabolic mirror, provides a completely Gaussian beam without imperfections, and with the previously mentioned diameter.

The entire system is placed in a Gimbal system, which help to point the laser beam to the right place, in this case the window of the fifth floor of the Fitz Hall at the University of Dayton, where the laboratory with the receiving optical systems is located. To properly direct this beam, there is a Cassegrain telescope which serves as a finder scope.

It is possible to select the wavelength of interest, turning off the other two, in this case, the wavelength we use is $\lambda = 1.064\ \mu m$, because it is a wavelength widely used in optical communication systems. The initial power of this beam is approximately $P_0 = 10\ mW$, so it can be considered as a low power laser.

2.3. Receiver platform – receiver optical systems

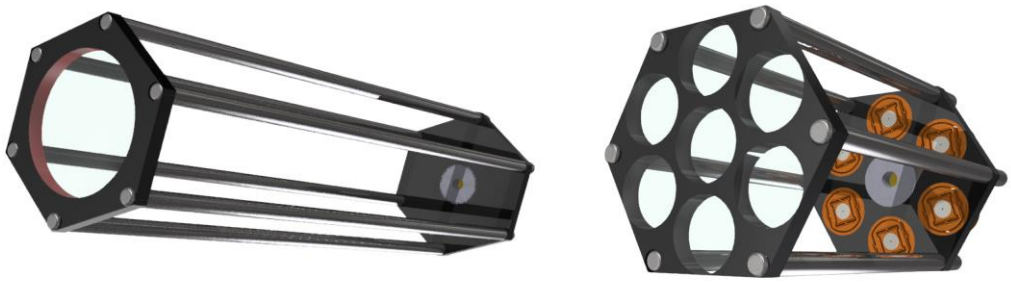

(a) (b)

Figure 9. Mechanical draws of the a) monolithic and b) tiled optical systems used for characterization of received power fluctuations in the receiver platform.

After the Gaussian beam produced on the beacon platform travels a distance of $L = 7\,km$ through atmospheric turbulence, it meets the Fitz Hall building at the University of Dayton. On the fifth floor of this building there is the window of the Intelligent Optics Laboratory, through which the Gaussian beam enters, finally this beam intercepts a set of different receiver modules that are intended to characterize atmospheric turbulence conditions using different methods.

Among the different optical receiver systems that we can find on the receiver platform, we can highlight the Cassegrain telescopes used for phase characterization of the received optical signal, the TILAS system used for different experiments, and particularly, the module used to compare power fluctuations induced by atmospheric turbulence, consisting of a monolithic telescope and a 7-channel multi-aperture array system, which will be described in detail in the following Sections (2.4 and 2.5). This pair of optical receiver systems are showed in Figure 9.

The main objective of this work is to experimentally determine which of the receiving optical systems (monolithic and tiled) has the greatest advantages, always having as a main figure of merit, fluctuations in the optical power received by both systems.

2.4. Monolithic Lens Receiver (MLR)

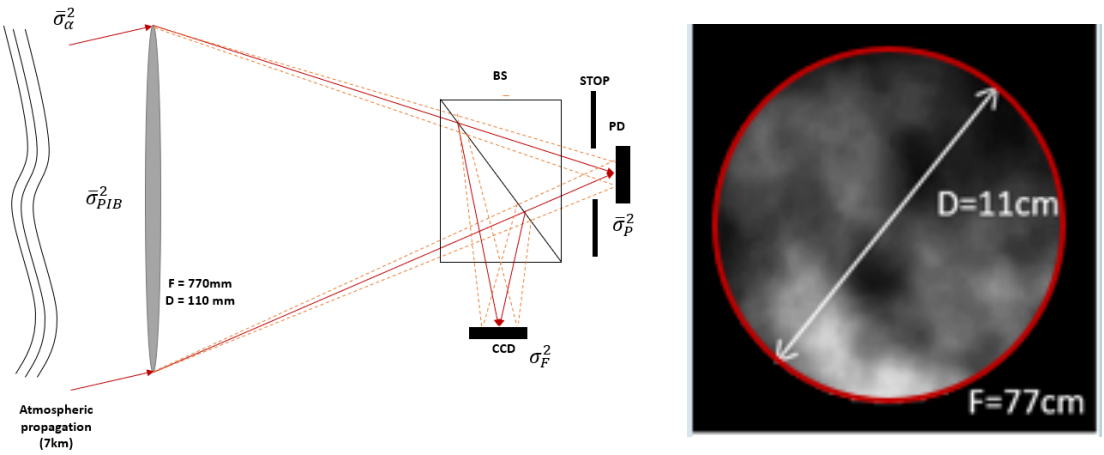

(a) (b)

Figure 10. Schematic representation of the monolithic optical system used in the series of experiments in this work. a) Side view of the monolithic system, b) Transverse view in the image plane. (Amplitude diagram for reference).

It is desired that the monolithic optical system has the same F number as one of the lenses used in the multiple aperture system, in order to preserve the reception angle in the Fourier plane in both cases, so we have searched from among all the options available in the laboratory, the most suitable monolithic system for these purposes. After said process, it was determined that the available monolithic system that best suits said characteristics is shown in Figure 10. This system has a focal length of F = 77 cm and a diameter of D = 11 cm, so the number F of this system has a value of N = 7, in Section 3.5 From this work the diameter of the initial entry pupil will be reduced, so this F number will have to increase.

The main characteristics of this monolithic optical receiver can be seen in Figure 10, where the experimental setup necessary to capture the power fluctuations induced with this system is shown laterally. On the other hand, the transversal view of the image plane of the optical arrangement mentioned in Section 2.1 can be observed. This view includes a simulated amplitude diagram, illustrative for comparison with the multiple

aperture optical system, in this diagram the fading regions and hotspots can be captured by the high diameter of this monolithic system.

Approximately in the Fourier plane of this instrument we have placed a has divider in order to couple two sensors that capture the optical signal in the focal plane instead of just one. One of these sensors is a CCD camera, which will have the task of finder scope for this monolithic system, with this we can correctly point to the beacon platform placed in the VA medical center, mentioned in section 2.2. The second one you have produced after the division, is captured by a standard photodiode power sensor, based on Silicon, which has an optical detection range of 400 to 1100 nanometers, so it is adequate to carry out these experiments. Note that this sensor has a diameter of D = 1cm, so it is almost a guarantee that the focal spot wander effect mentioned in Section 1.13 will not significantly affect the variation in optical power due to atmospheric turbulence in the plane. telescope receiver. The information transmitted by the photo detector used to capture variations in optical power in the monolithic system receiver, will be processed by a microcontroller, which is described in Section 2.7.

2.5. Multi Aperture Receiver (MAR)

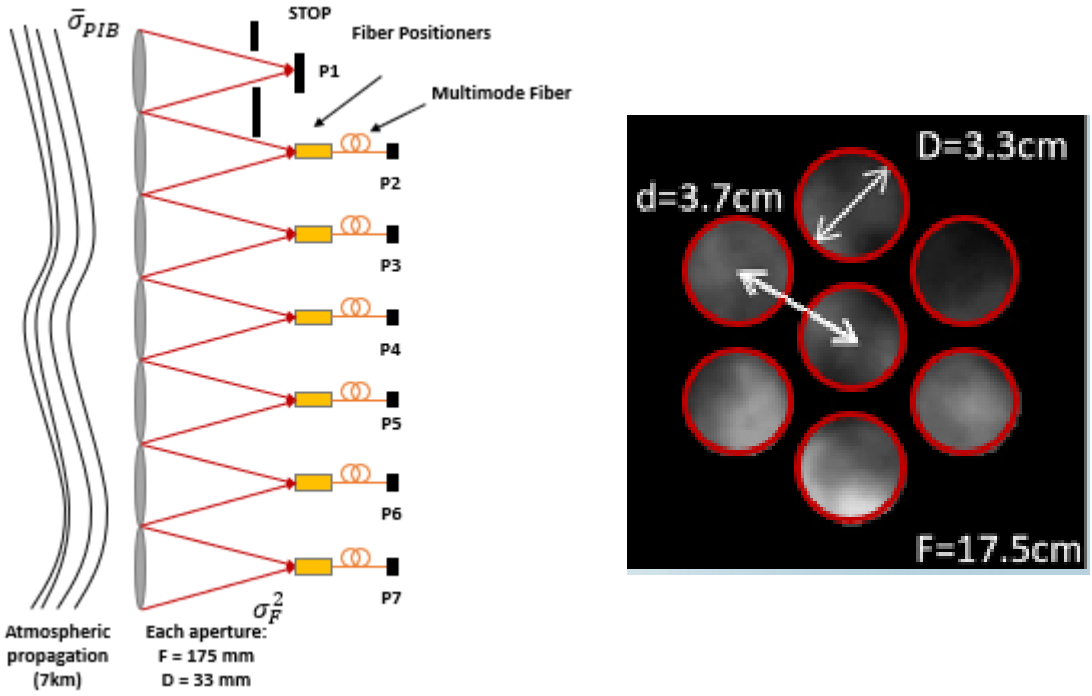

(a) (b)

Figure 11. Schematic representation of the multi-aperture optical system used in the series of experiments in this work. a) Side view of the monolithic system, b) Transverse view in the image plane (phase diagram for reference).

As shown in Section 1.14, by increasing the collection area in a receiver system used to capture optical power fluctuations induced by a laser beam propagating through atmospheric turbulence, the variance of the mentioned detected power will be reduced, therefore, is desirable to have optical instruments with a large collection diameter in order to mitigate the effects of atmospheric turbulence and, resulting in a reliable optical information transfer.

However, building an optical receiver system with a big diameter implies some technical and manufacturing complications [45,46], among which the polishing of optical elements with big curvatures stands out, this

can be avoided if the focal length of that optical element is increased as well, resulting in a receiver system with a large diameter and a large collection area, but also with a large focal length. A large focal length in an instrument has another kind of problems such as the focal spot wander described in Section 1.13, which worsens as the focal length of the receiver increases, resulting in a non-reliable option for fiber coupling. In other hand, an optical collector with a large focal length results in an instrument not compact and difficult to implement in certain circumstances, for example, when implementing an instrument with these characteristics on an airplane is desired. In some experiments, a partially coherent optical system has been used to have a better performance on the aperture averaging without increasing the collection area of the optical receiver [47]. However, there is a way to increase the collection area of an optical receiver, reducing the power fluctuations induced by atmospheric turbulence, without compromising its focal length: *multi aperture array optical receivers*.

Modern astronomy currently proposes the use of receiver systems with a big collection area, by implementing multi aperture array systems that uses a geometrical arrangement of lenses with a small diameter and focal length on the same plane [48-50], increasing the collection area of the entire system, but preserving the focal length of one of its individual components. The first similar arrangement known could be the *Hartmann test* proposed in 1900 [51,52], a system used to measure the wavefront produced by an optical element and determine its aberrations and surface errors. In 1971 Patt and Shack proposed a similar model, based on an arrangement of lenses in the same transverse plane, which is useful for the measurement of collimated beam fronts, obtaining the curvature of the eye, among other applications, this system is called *lenticular Hartmann screen* [53] and it is a practically identical receiver than the used in this work to measure the optical power fluctuations induced by atmospheric turbulence.

An illustrative diagram of the Multiple Aperture Receiver (MAR) used in the experimental series of this work can be seen in Figure 11, which consists of seven lenses placed in a hexagonal arrangement on the same plane, six of them (P2-P7) are coupled to an multimode optical fiber with a core diameter of $a = 100\ \mu m$ and a numerical opening of $NA = 0.26$, by using *x, y and z fiber positioners,* which have three degrees of

freedom, so the tip of the fiber can be moved manually on the x, y and z axes, advantage that will be used to perform the alignment described in the following Section. Finally, this light coupled to the optical fiber is transmitted to a photodetector, a subsystem that will be described in detail in Section 2.7. The seventh channel (P1) does not use a fiber coupling but is directly captured by a photodetector. The information transmitted by these photodetectors will be showed by different display interfaces such as oscilloscopes and commercial optical power meters, however, the processing and combining of these signals will be done digitally, except for the experiments shown in the Section 3.4 where the combination of beams is done with fiber combiners.

On the other hand, in the cross-sectional view of Figure 11, this hexagonal arrangement can be seen and how it intercepts the same amplitude diagram shown in Figure 10 for the monolithic system. It can be seen that the fading regions and hot spots are mostly captured by the complete system, however, some of the lenses in the array capture hot spots and other fading regions, so it can be expected that each lens separately presents a higher variance of the received optical power, than with the averaged entire complete system, in other words, by increasing the number of apertures used and doing their corresponding average process, we will notice a reduction in the variance of the received power, resembling the aperture averaging effect , where this variance of optical power is reduced as the collection diameter of the receiving optical system increases, therefore, if the propose is to use the aperture averaging theory to describe the reduction of fluctuations in the received optical power due to the increase in apertures averaged, an effective diameter should be defined that represents the diameter of the total collection area achieved with the adding of individual small lenses.

The systems that integrate a fiber coupling have the advantage that they can also be used as optical transmitters, thus being able to increase the possibility of applications of these instruments, one of them being the alignment shown in the following Section. In fact, there is currently an important demand for multi-fiber array laser transmitter systems used for remote spectroscopy, active imagers, laser tracking and particularly, free space communications [54,55], this systems normally integrate *active fiber actuators (AFA)*

in the focal spot of each aperture, in order to compensate for wavefront aberrations caused by atmospheric turbulence, thus compensating for fluctuations in optical power induced by turbulence, this is known as *adaptive optics* and there are different methods used in practice to carry it out this process, one of the most effective and popular is de SPGD method [56].

The experimental procedures of this work have been carried out with x, y and z fiber positioners in the the multiple aperture system used as an optical receiver.

With all the above information we can list the following advantages of multi-aperture receiver systems:

The aperture averaging effect is reduced by increasing the collection area of this optical system, simply by implementing more individual apertures in the receiver plane. Resulting in a scalable and compact system, with a reduced focal length.

At the same time, these multi aperture array receivers have the advantage of being able to be used as receivers and transmitters because its fiber coupling, this is possible due to the fact that the effect of focal spot wander described in Section 1.13 is reduced for small focal distance lenses, therefore, in theory, most of the light captured with this optical receiver will be successfully coupled to a multimode optical fiber with a large diameter compared to single-mode fibers, this assumption will be debated in Section 3.2.

2.6. Assembly and alignment of a Multi Aperture Receiver (MAR)

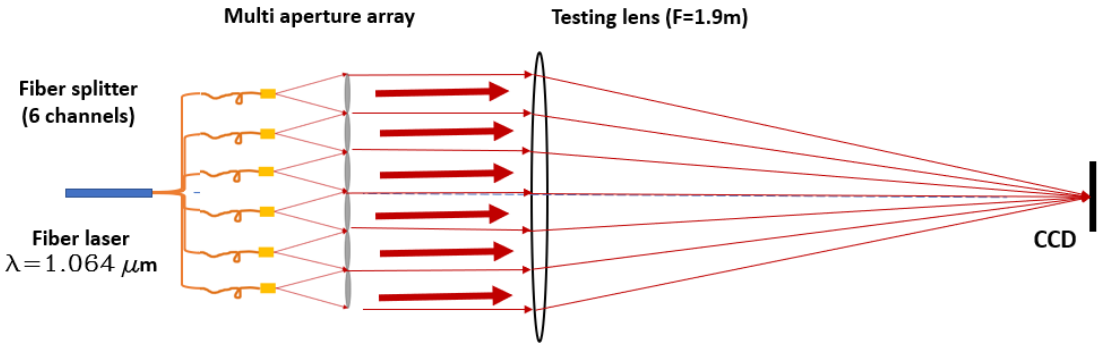

Figure 12. Multi aperture receiver ideally aligned, all the apertures are perfectly collimated and parallel to each other.

Despite all the advantages of a multi-aperture receiver for detecting optical power fluctuations induced by atmospheric turbulence, mentioned in Section 2.5, this optical system has several disadvantages to consider before implementing it. One of those disadvantages is the complexity of each mechanism and opto-mechatronic component, particularly the x, y and z fiber positioners, used to align the apertures of this receiver.

Originally this optical system, shown schematically in Figure 9b), is unassembled and the assembly process can take a couple of working days, however, this is not complicated if the optomechanical parts are properly manufactured. Particularly, two multi aperture array receivers where assembled and aligned in this work, in one of those, the mechanical parts of the tube of this optical system were designed for a longer wavelength than the used in these experiments ($\lambda = 1.06\ \mu m$), so, the x, y and z fiber positioners had to be corrected, in order to reduce their length, placing the tip of the optical fiber at the correct focal length of each sub aperture ($F = 175\ mm$).

Once this optical receiver has been assembled, it is necessary to align it using the x, y and z fiber positioners. As mentioned in Section 2.5, each aperture has a x, y and z fiber positioner, with three degrees of freedom, that allows the positioning of the multimode optical fiber tip at the correct focal length and perfectly centered on the optical axis of the small lens of each sub aperture. This alignment will allow the light collected by the optical fiber in each channel to be coupled optimally, resulting in all channels receiving the same average optical power, which occurs when all apertures are aligned parallel to the same optical axis, on the same focal plane.

This alignment can be performed if this optical receiver is used as a transmitter, for this purpose, a fiber laser with a wavelength of $\lambda = 1.06\ \mu m$ is connected to an eight-channel beam splitter, and six of them are transmitted to the optical fibers of the multi-aperture system, if the alignment of this receiver were perfect, the propagation through each of the apertures would be completely collimated and all these collimated beams would propagate parallel to each other. With the help of a collimating lens of $F = 1.9\ m$, it is possible to capture all these collimated beams, and in the focal length of that lens, a central point must be observed product of the superposition of all the collimated beams in a same focal plane. This can be seen in Figure 12.

In practice, once the multi aperture array system is assembled, the initial alignment is poor and this process must be done manually by using x, y and z fiber positioners, which is why only six of the seven apertures (the ones of the periphery) will be aligned, the seventh aperture (the central one), as described in Section 2.5, is not coupled to a fiber and its alignment is much easier since the photodetector just needs to be placed placed approximately in the focal plane of the central aperture, and due to its large size, all information will be received despite poor alignment and the focal spot wander effect. Therefore, we can ensure that the fluctuations detected with this channel will be the power in the bucket fluctuations without any loose or any extra fluctuation induced.

To achieve the alignment shown in Figure 12, it is first necessary to align the collimating lens.

We can divide this procedure into one of the following four steps:

1)

First, the tip of a fiber optic laser is placed approximately at the focal distance from the collimating lens, this laser has a numerical aperture of $NA = 0.12$, and a core diameter of $d_c = 2.5\ \mu m$, so that the coherent light produced by this laser will be propagating, forming a cone of light with an angle defined by the numerical aperture. After this, a beam splitter is placed which will have an important function later. After the light propagates a distance of $F = 1.9\ m$, it intercepts the collimating lens, which should produce a completely collimated beam if the tip of the fiber is in the focal plane of this lens. This will be tested with a sufficiently large shear plate interferometer [57], which will also help to observe and correct slight unwanted tilts in this lens, the interference pattern desirable will be composed of completely vertical and parallels lines. This first step is showed in Figure 13.

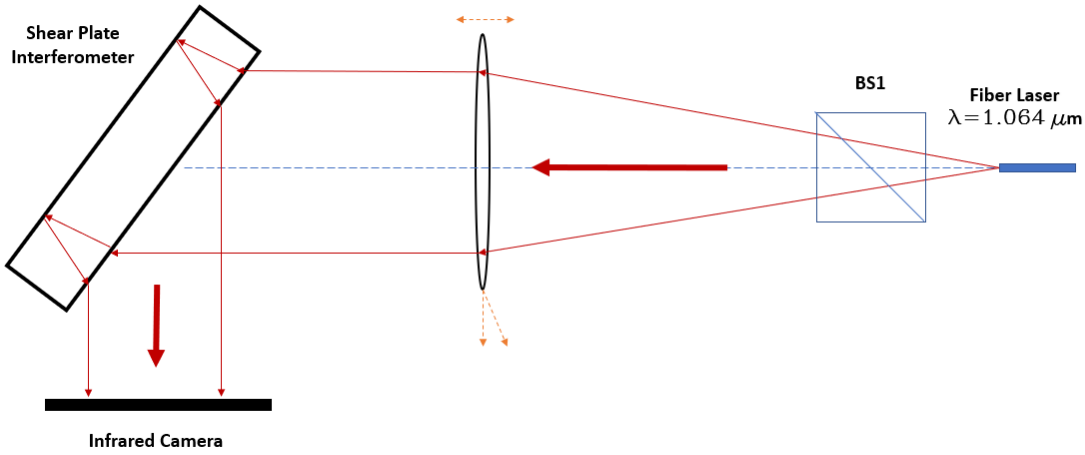

Figure 13. First step for the alignment of a multi aperture array system, placing the collimating lens and testing it with a shear plate interferometer.

2)

Once the collimating lens has been properly aligned, the cameras that captures the light beams from the multi aperture array system, can be incorporated to the system. These cameras have to be placed in the focal plane of the collimating lens, which is why for this second step it is necessary to keep the components of the previous step, exchanging the shear plate for a corner cube mirror (retroreflector), which will reflect the light by the same optical path from where it originally traveled, producing a small spot at the output of the laser and another at the second arm of the beam splitter. In the second path produced by the beam splitter must also be placed a second beam splitter, as seen in Figure 14, which gives the possibility to transmit that beam to two different cameras, one of them will be coupled to a microscope objective with a magnification of $M = 4x$, with this, the alignment can be performed more accurately.

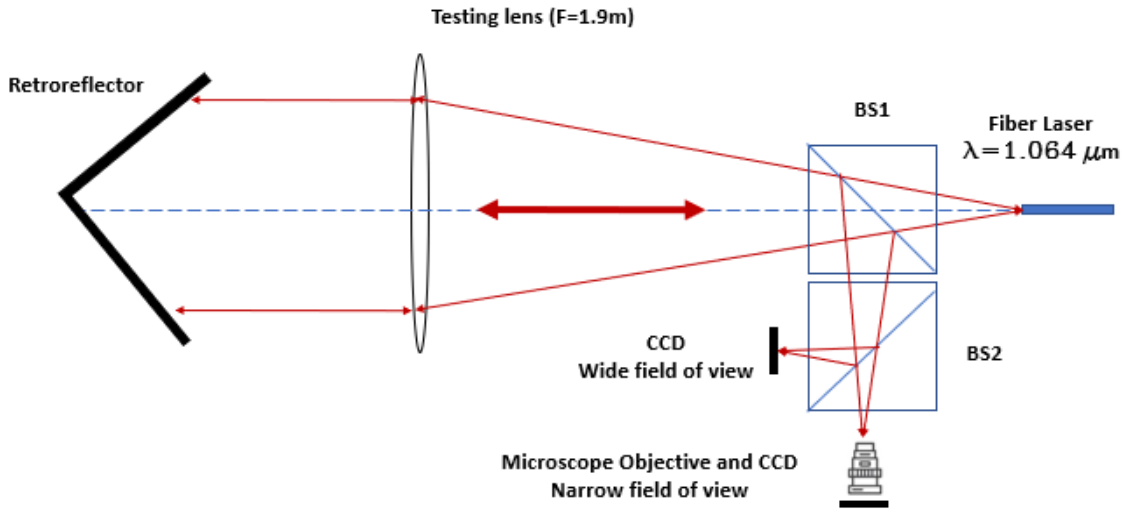

Figure 14. Second step for the alignment of a multi-aperture optical system, placing the CCD cameras and the microscope objective in the focal plane of the collimating lens.

3)

After the two cameras used in this arrangement are correctly positioned in the focal plane of the collimating lens, it is possible to remove the optical fiber used and finally place the multi-aperture array in its transmitter configuration, in order to align each of its channels with respect to the rest, with the help of its x, y and z fiber positioners. To do this, one of these channels, in this case the P5, is perfectly aligned and taken as a reference, the rest of them are aligned with respect to that channel. This arrangement can be seen in Figure 15.

The information captured by the CCD cameras is transmitted to a screen that allows the observation of the superposition of the generated beams, for a better explanation of this process, Figure 16 must be observed.

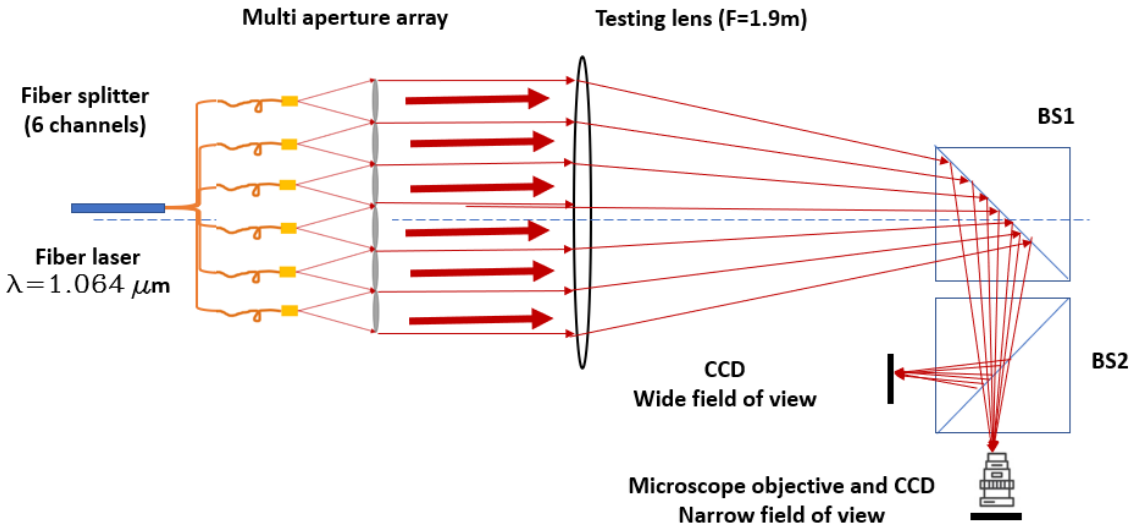

Figure 15. Third step for the alignment of a multi-aperture system, aligning the all the sub apertures.

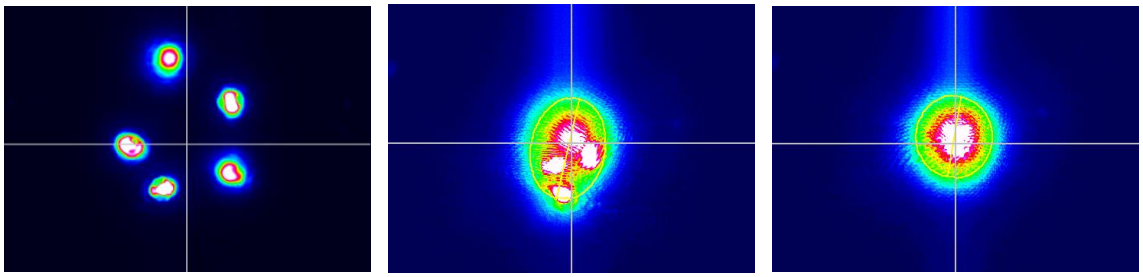

(a) (b) (c)

Figure 16. Alignment of a MAR. a) Scattered focal spots of different sizes, b) nearby focal spots, c) fully spotted focal spots with the same size (sub apertures aligned).

This third step is the most important because it is the necessary step to align the multi-aperture array system, so it is worth illustrating the two processes for the alignment mentioned above: defocus and tilts. In the first case, the tip of the optical fiber must be placed in the focal plane of the small lens, in order to achieve this, the fiber tip can be moved on the z-axis of the lens until a perfect image of the tip of the fiber is formed in the CCD camera. This is a qualitative process and will depend on the accuracy of the operator to perform it properly. On the other hand, the second case corrects the tilts of each sub aperture, and this is achieved by positioning the tip of the fiber on the same optical axis of the lens, by means of translations on the x and y axis.

4)

The final step for the alignment of this optical system is to place the finder scope that will help to locate the beacon platform from the receiving plane of the optical arrangement mentioned in Section 2.1. For this, all the components used in the previous steps of this alignment so far are removed, knowing that all the sub apertures of the multi aperture receiver have been correctly aligned. After this, the retroreflector is placed in the front of the MAR.

By using only as reference the fifth channel (P5), a perfectly collimated beam is propagated to the retroreflector, and finally it will be captured by the finder scope located in the same plane of the MAR, which will be connected to a camera that will show in a screen, the image of the tip of the optical fiber, which has to be positioned in the center of that screen, by moving the tube of the Finder scope on the x and y axis. The image of this fiber tip, will be the reference point used to point the receiving system, reason why the contour of this image is drawn on the screen as a target, and it will also help us to verify experimentally if the focal spot wander exceeds the size of this fiber. The above can be seen in Figure 18. In Section 2.7, this finder scope will be explained with more detail.

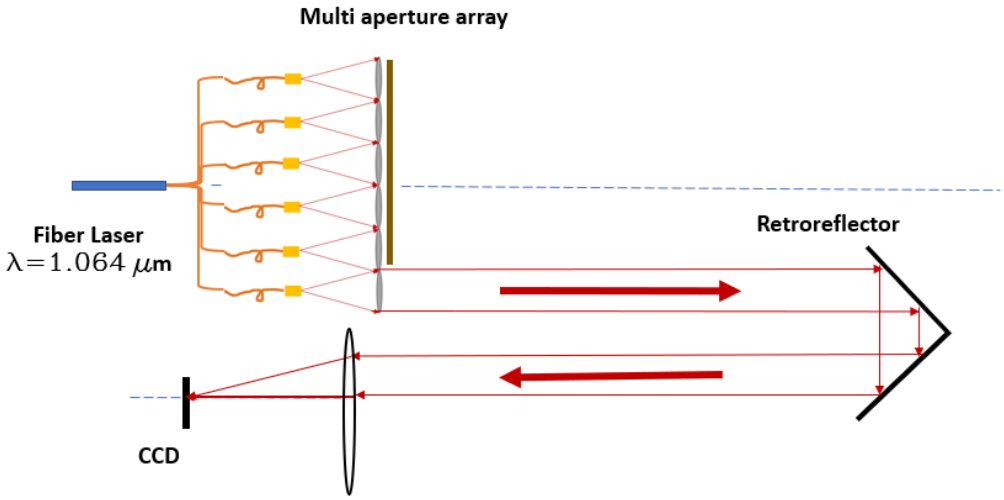

Figure 17. Fourth step for the alignment of a multiple aperture optical receiver, placing the finder scope.

Once the alignment of this optical system has been achieved, it can be placed in the receiving plane of the experimental arrangement mentioned in Section 2.1, to measure optical power fluctuations induced by atmospheric turbulence. However, the final equalization of all the channels is performed using that atmospheric testbed. The goal is to have the same average power received with each of the sub apertures. Figure 19 shows the fine equalization achieved of this receiving optical system, while the modifications that were made in each channel to achieve a good equalization are indicated with arrows.

The average power values obtained by one-minute measurements, are linearly related to the voltage values shown in Figure 19. Section 2.7 explains in detail this conversion and in general the process for acquiring the received optical power fluctuations, as well as its variance, for both receptor systems (monolithic and tiled).

In the case of an active fiber positioner, the degrees of freedom are increased since it is possible to modify not only the transverse position of the optical fiber with respect to the focal plane of each lens, but also the positioning angle of the multimode optical fiber tip, resulting in a much more complex system with 5 degrees of freedom instead of 3.

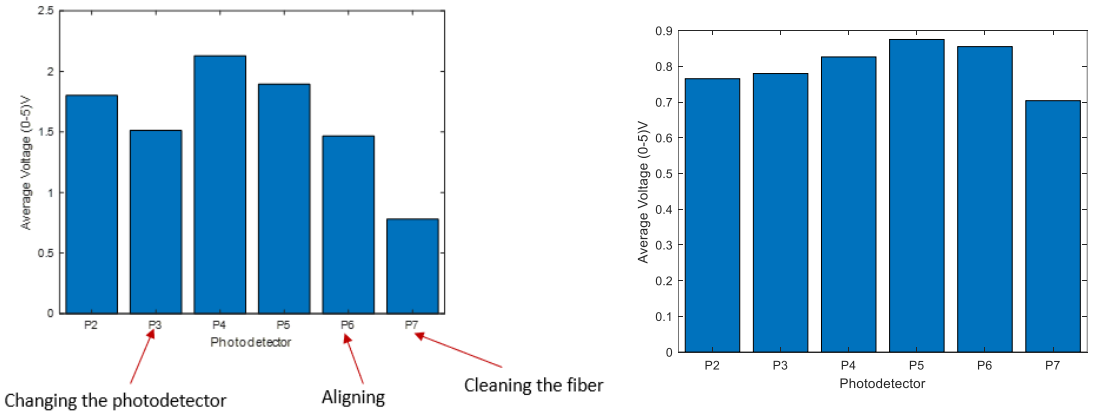

Figure 18. Equalization of the average optical power received in each sub aperture of the multi-aperture receiver. a) before equalizing, b) after equalizing.

2.7. Optimization of power fluctuations received and acquisition of data

When the optical devices described in Section 2.3 are correctly aligned, it is possible to place them in the image plane of the atmospheric arrangement shown in Section 2.1. Once this is done, it is necessary to search through the window, with the help of the finder scope of each receiving device, the beacon platform located in the roof of the VA medical center, the best way to ensure that our receiving devices are truly pointing to the laser source, is observing the pattern of the screen assigned to the finder scope of the multiple aperture system described in Section 2.6, which will be saturated vertically due to the incidence of the Gaussian beam of $\lambda = 1.06\ \mu m$ in the camera's optical sensor of the finder scope, even though it is not very powerful.

If saturation is not observed on the screen, the power of the laser may not be sufficient to, after atmospheric propagation of $L = 7\ km$, be detected by the sensors of the receivers, then it will be necessary to remotely increase the electric current supplied to the laser to carry out its propagation process, normally a current of $I = 100\ mA$ is enough. However, in case of a suspiciously low power detected in our optical systems, the main reason for this problem is a misalignment between the laser radiation source and the optical receiver to be used. To ensure maximum received power through the alignment of these systems, a high-precision Gimbal, mentioned in Section 2.2, is used, or a slight tilt is given to the receiving optical systems used in order to be positioned on the same optical axis of the laser beam, this source will be practically at infinite for the finder scope, and its image should fit perfectly in the fiber tip representation on the screen that was previously drawn. This process is quite qualitative and depends on the observation of the operator of these instruments, however, it is easily achievable thanks to the remote control of the beacon platform, and the sensitivity of the CCD camera of the finder scopes which are easily saturated with optical powers received (in order of micro watts) . This process can be visualized in more detail in Figure 20.

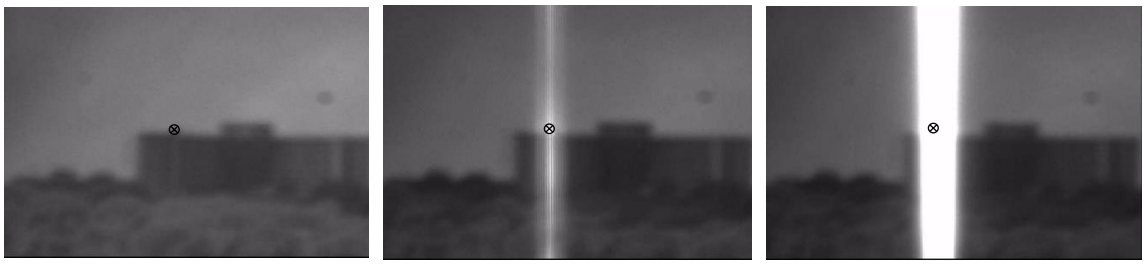

(a) (b) (c)

Figure 19. Pointing of the multi aperture array receiver using a finder scope a) Out of axes, b) Almost on axes, where the screen is almost, c) On axes, where the image finally gets saturated. The circle in the middle is the target, and at the same time is the image of the multimode fiber tip on the focal plane of the aperture P5.

Another technique for qualitative analysis of the received optical signal and the maximization of this by alignment, is using an oscilloscope that shows us the fluctuations of the received signal due to atmospheric turbulence, and how these change by optimizing the position of the Gimbal and the alignment of receiving optical systems.

Once the optical power received in the focal plane is optimized, and the alignment of the atmospheric arrangement is guaranteed, it is necessary to prepare the interface for the visualization and acquisition of the power fluctuations captured by the optical sensors of each aperture. This receiver module has two apertures using a standard photodiode power sensor of $D = 1\ cm$, one for the monolithic system and one for the central sub aperture of the multi aperture array, on the other hand, the other six apertures of that multi aperture receiver are captured, as mentioned in Section 2.5, by an optical fiber of $d = 100\ \mu m$, which transports the captured signal, to a detector which transforms the optical power into an analog voltage that can be processed with a microcontroller.

This microcontroller is also known as an analog-to-digital converter and must meet several requirements to be implemented in this array, one of those requirements is to have at least 8 analog channels to capture

the power information received with all the optical apertures. Another of the necessary characteristics of this analog-to-digital converter is to have a suitable acquisition frequency to capture the fluctuations of received optical power [58], that sometimes will change very fast, when the atmospheric turbulence is strong. The first device proposed for this work was a low-cost microcontroller board which a sampling time of 4 milliseconds between each measurement by measuring 8 channels, however, in conditions of strong atmospheric turbulence, this sampling value will not be sufficient, so this low-cost board was replaced by an NMC® microcontroller, which offers a sampling frequency for 8 channels of 0.2 milliseconds.

The digital to analog converter will provide a time graph of -10 to 10 V, which will represent the value of the digitized optical power as a function of time. To obtain the measurement of actual power received at a given time it is possible to multiply this voltage value by a constant amount that depends on the gain of the detector, its responsivity (depending on the wavelength of the signal), and a gain factor. However, the figure of merit to be used in this work is the normalized variance of the received power information, so the actual optical power values are not of interest and these will be normalized.

Figure 21 shows the temporal evolution in the optical power fluctuations detected in the monolithic receiver, described in Section 2.4, for different values of atmospheric turbulence represented by the factor Cn^2. These measurements are usually carried out for a time of $t = 1\,min$, because also the values of Cn^2 provided by the scintillometer in the laboratory, are updated every minute, large enough period to average the behavior of the received power fluctuations during this time. This exposure time is adjustable with the microcontroller software (Python). This time can also be digitally trimmed after obtained. The fluctuations on strong turbulence has peaks of intensity very clear to see comparted when weak turbulence conditions, this is going to increase the normalized standard deviation of the data.

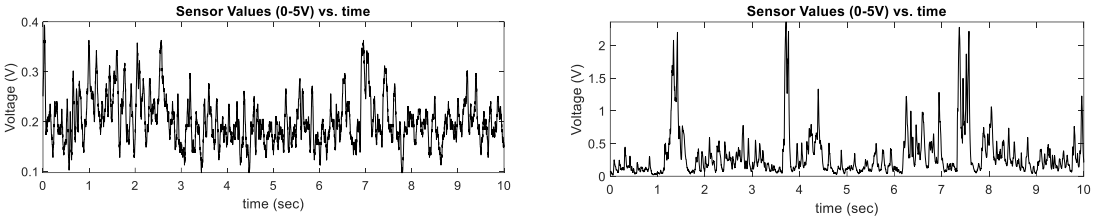

(a) (b)

Figure 20. 10 seconds measurements of power fluctuations observed with a monolithic aperture receiver of $D = 11\ cm$ for a) weak turbulence $Cn^2 = 3.31e^{-15}\left[m^{-\frac{2}{3}}\right]$ and b) strong turbulence $Cn^2 = 1.226e^{-14}\left[m^{-\frac{2}{3}}\right]$

Combining the information of these signals is necessary for some of the experiments performed, so in section 3.4 the advantages and disadvantages of combining signals digitally once captured or combining them optically using fiber optic combiners are explored.

Once the signals are correctly captured and digitized, they can be processed to obtain useful and descriptive information about the associated atmospheric turbulence conditions for the corresponding measurements, using the experimental methods described in the next chapter.

CHAPTER III EXPERIMENTAL METHODS FOR ATMOSPHERIC OPTICAL RECIEVERS

In this chapter, several different experiments are proposed to determine the performance of the two receiver optical systems presented in Section 2.1, placed in the image plane of an optical configuration where a Gaussian beam with $D_0 = 2.5\ cm$ and $\lambda = 1.064\ \mu m$ propagates through an atmospheric channel of $L = 7\ km$ with different conditions of atmospheric turbulence. The main figure of merit used for these purposes will be the normalized variance of the power fluctuations observed by the experimental arrangement described in Chapter II. If the normalized variance has a small value, this means that the optical power information obtained with the receiving system is stable and therefore reliable, so to determine if a collection method is good or not, this statistical parameter will be the main indicator.

Section 3.1 shows the effect of using a multimodal fiber coupling to transmit the information received in the multiple aperture receiver system, this was achieved by replacing the photo detector used to measure Power in the Bucket fluctuations for the central aperture of the Multi Aperture Receiver system, by a x, y and z fiber positioners to transmit the optical information to the fiber optics with a much more smaller diameter than the photodetector originally used. The increase in power fluctuations expected when decreasing the reception radius in the Fourier plane could be directly related to the focal spot wander effect.

The experiment proposed in Section 3.2, shows the relationship between the increase of sub apertures used in a multiple aperture system, and the decrease in the average power fluctuations detected in the image plane of the optical system used (tiled). This procedure can be considered as an example of aperture averaging where the diameter of the optical system is not increased, but its total area, therefore, it is necessary to define an effective collection diameter for each case, from 1 to 6 averaged sub apertures. It is important to mention that in this case, the information detected by each sub aperture was coupled to a different fiber with its own power meter, so the treatment of the information received was carried out using a digital combiner system.

In the experiment number 3, showed in Section 3.3, the possibility of using a fiber combiner instead of a digital combiner to perform the statistics of power fluctuations detected in the image plane by the multiple aperture system, is explored. The objective is to verify if in any of the two cases the fluctuations of received optical power are increased, and what happen with the average optical power received in this multi aperture system when using variants of aperture combinations.

For the fourth experiment, showed in Section 3.4, we increased the collection area of the monolithic receiver, by using masks with different sizes and shapes, trying to preserve the value of Cn^2, in order to directly observe the reduction in the normalized variance of the power fluctuations received with that optical receiver, when its area is reduced.

The last experiment, in Section 3.5, proposes a method to estimate the horizontal wind speed of the atmospheric turbulent medium by which our Gaussian beam propagates. This process is carried out obtaining the cross-correlation function between different channels of the multiple aperture optical system.

3.1. Measured power fluctuations received in an aperture with fiber coupling and with a photodetector

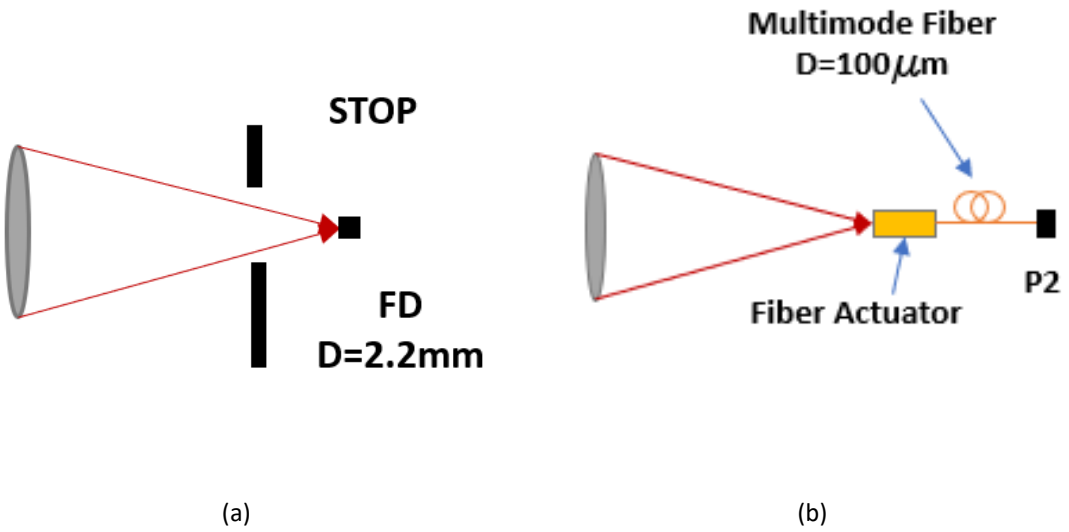

Figure 21. Configuration of optical power detection systems. a) Using a photodetector (Ø = 2.2 mm), b) Using a multimode fiber coupling (Ø = 100 μm).

In the first experiment we analyzed the Multi Aperture Receiver which, as mentioned above, has six sub-apertures, which couple the light received in the focal plane to fiber optics. However, the central channel has a Ø = 1cm diameter photodetector which captures power fluctuations directly without any fiber optic coupling. In Figure 22, a schematic diagram of these configurations can be seen.

One way to verify that the coupling to optical fiber does not induce an extra variation of the received power, it is to analyze the normalized variance obtained with the central channel and one channel on the periphery with coupling to multimode fiber for different cases of atmospheric turbulence , in favorable and in poor condition. These measurements have been

made during t = 1 minute and can be seen in Figure 23. As shown in this graph, the channel that includes multimode fiber optic coupling has a much higher normalized variance than in the case of the central channel that performs measurements with a standard photodetector.

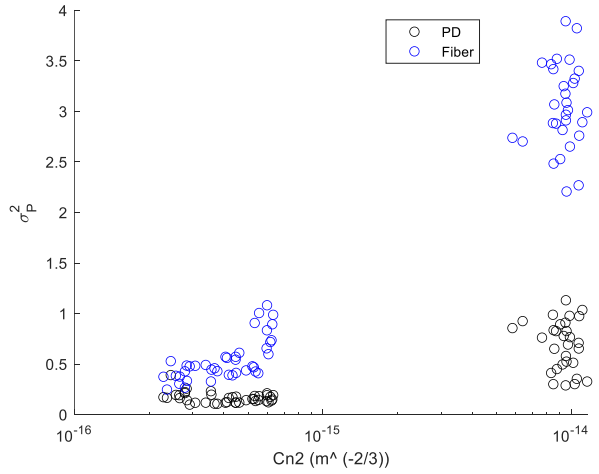

Figure 22. Normalized variance of received optical power obtained experimentally, for different atmospheric turbulence conditions, using a conventional photodetector (Ø = 1 cm), and a photodetector coupled to multimode fiber (Ø = 100 μm), in the focal plane of a $D = 3.3cm$ and $F = 17.5cm$ lens.

The above may be due to different reasons, however, the first assumption is that due to the effect of focal spot wander, the wave in the focal plane cannot be completely coupled in the fiber and thus, some information on the received power is lost. , increasing its normalized variance. To confirm this hypothesis, we calculate the size of the focal spot generated after a Gaussian beam ($\lambda = 1.064\ \mu m$) with a plane wavefront is collected by a lens of $D = 3.3cm$, for this, we use the expressions (29) and (31), with which we find that this focal spot will have a size of $\omega\ (F) \approx 5\mu m$. This value is significantly less than the $\emptyset = 100\ \mu m$ diameter of

the core of the multimode optical fiber used (in the case of a single mode fiber this would be totally different). However, when the effects of atmospheric turbulence are introduced, this diameter observed during a certain exposure time will tend to increase as a function of atmospheric turbulence due to the focal spot wander effect, described in Section 1.13. In Figure 24, the behavior in the standard deviation of the diameter of the focal spot in both optical receptors (monolithic and tiled) can be observed on a logarithmic scale, as a function of the C_n^2 parameter. It can be seen that the standard deviation of this focal spot is on the order of $1e^{-6} \leq \sigma_F \leq 1e^{-5}$, for the range of atmospheric turbulence commonly present in the intelligent optics laboratory ($1e^{-16} \leq C_n^2 \leq 1e^{-14}\left[m^{-\frac{2}{3}}\right]$), so in neither case can it be thought that this effect will be sufficient to prevent the coupling of the electromagnetic wave captured to a multimodal fiber optic with a core diameter of $\emptyset = 100\ \mu m$.

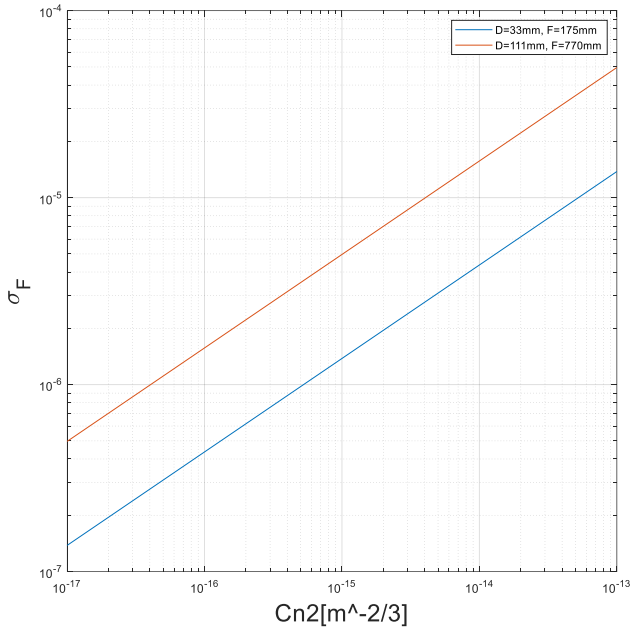

Figure 23. Predicted Focal Spot Wander for a Monolithic Lens Receiver (red line) and one of the apertures of a Multi Aperture Receiver (blue line) under different turbulence conditions.

So, if the probability that the focal spot wander affects the variance of the optical power detected with the Multi Aperture Receiver channels that include fiber coupling is very low, the following hypothesis to explain the difference in normalized variance observed in Figure 23 could be that the photodetector used in the central sub-aperture of the Multi Aperture Receiver ($\emptyset = 1\ cm$), provides a lower sampling frequency than that provided by the fiber optic photodetector with a much smaller size ($\emptyset = 2.2\ mm$). In order to see this, we observe Figure 25, were the optical power fluctuations detected in both cases are shown, during $t = 0.5\ seconds$, in this experiment, the atmospheric turbulence has a value of $C_n^2 = 9.042e^{-15}\ [m^{-2/3}]$ (strong turbulence).

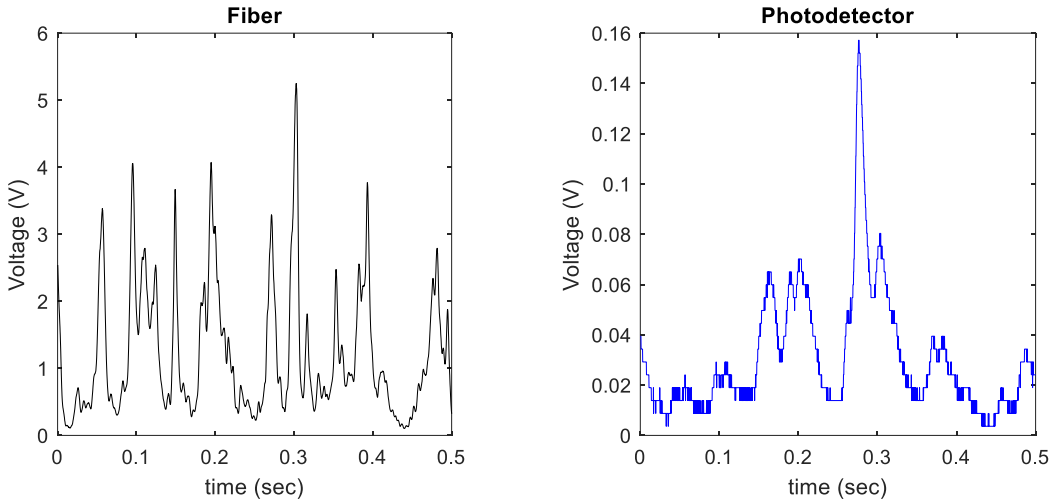

Figure 24. Optical power measurements for $t = 0.5\ seconds$, using a) Multimode fiber optic coupling, b) photodetector (Ø = 1 cm).

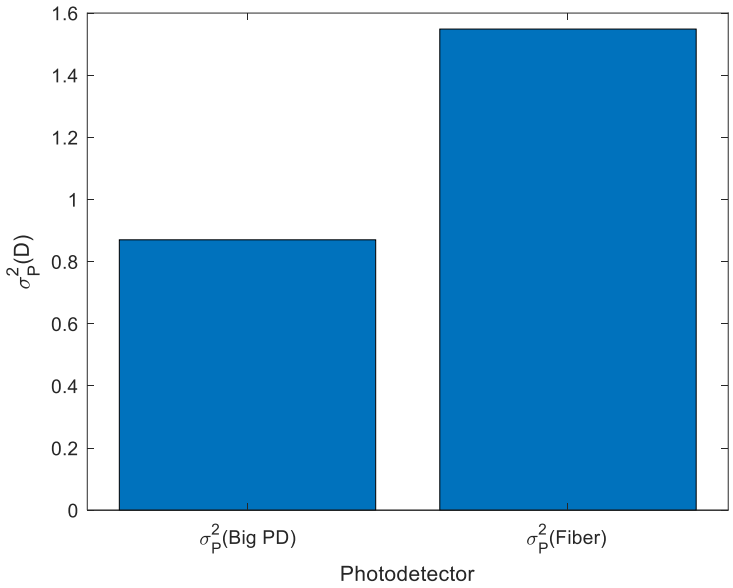

Figure 25. Normalized variance of the received optical power in a) A photodetector of Ø = 1cm and b) A photodetector with fiber optic coupling. For $C_n^2 = 9.042\, e^{-15}\ [m^{-2/3}]$ (Strong Turbulence).

As can be seen, in the case of the central sub-aperture that incorporates a common photodetector, the signal is captured with a lower acquisition frequency than in the case of the fiber optic detector, this means that as the size of the detector, this decreases the sampling frequency, therefore, the normalized variance of the detected information will be artificially decreased, in Figure 26 The variance of the optical signal detected in both cases can be observed, which confirms the previous hypothesis.

Once it has been discovered that the fluctuations in optical power are artificially reduced by increasing the size of the detector used in each sub-aperture, we proceed to change the photodetector of the central channel, for one that measures $\emptyset = 2.2\ mm$. In the Figure 27 it is possible to see that the normalized variance increases when we change the photodetector, reaching a very similar value to that offered by the sub-apertures that incorporate a

multimode fiber optic coupling. This is good news, because it confirms that the multimode fiber optic coupling does not increase power fluctuations due to the focal spot wander effect, with which we can say that all the received power will be transmitted to that fiber optic regardless of the atmospheric turbulence conditions.

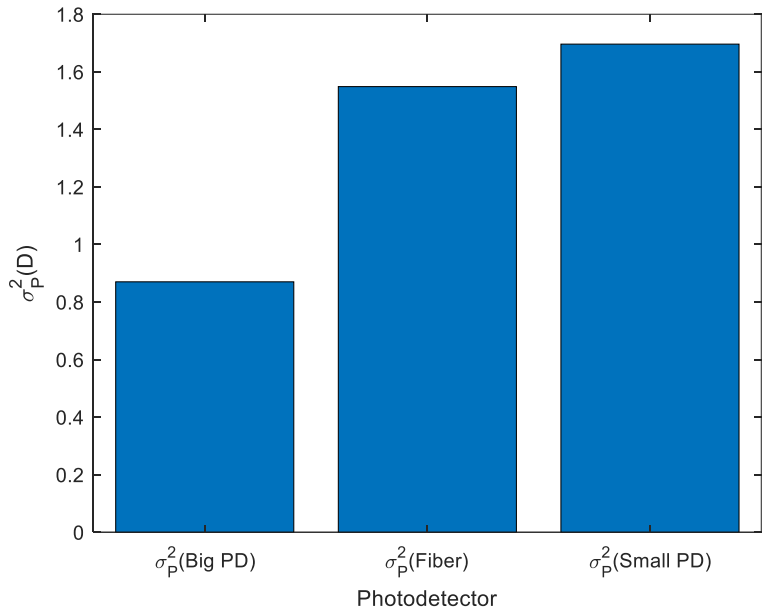

Figure 26. Normalized variance of the received optical power in a) A photodetector of Ø = 1cm, b) A photodetector with fiber optic coupling and a) A photodetector of Ø = 2.2 mm. For $C_n^2 = 9.042\ e^{-15}\ [m^{-2/3}]$ (Strong Turbulence).

3.2. Power fluctuations reduction as apertures are increased in a tiled optical receiver

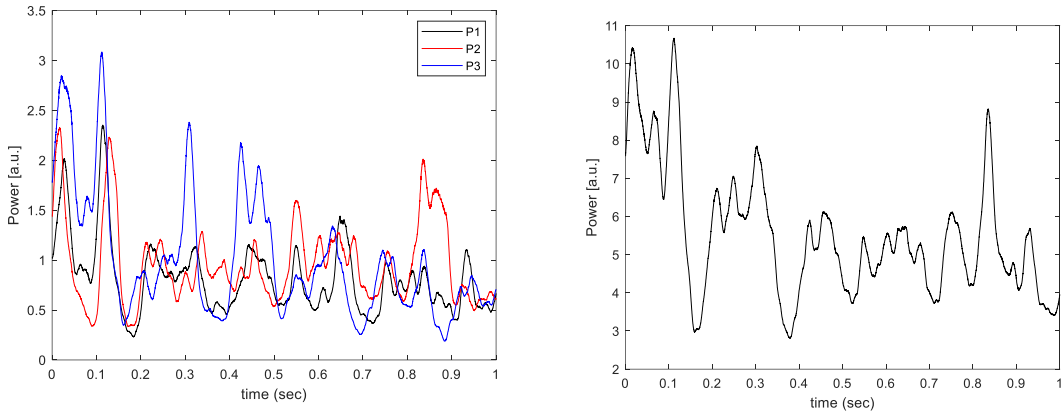

(a) (b)

Figure 27. Temporal behavior of the power fluctuation detected by a) 3 separated apertures and b) the sum of the 6 sub-apertures.

Measurements in the normalized variance of the detected optical power using an aperture with coupling to a multimode fiber, have been made using a single sub-aperture of the multi aperture fiber array. However, this optical system has six sub-apertures with fiber coupling, which can decrease the normalized variance of the total power received, by increasing the number of sub-apertures averaged. In order to achieve this, a digital combination of the time dependent power obtained by each sub-aperture for one minute, will be performed.

Figure 28a) shows the temporal behavior of the optical power $P_i(t)$ that has been coupled to the multimode fiber for three different openings $(i = 2,3,4)$ during $t = 1\ second$. In this case, these data were recorded while the Scintec BLS 2000 scintillometer measured a path-averaged refractive index structure constant of $Cn^2 = 4.52\mathrm{e}^{-16}\ \left[\mathrm{m}^{-\frac{2}{3}}\right]$ (weak turbulence). Assuming homogeneous turbulence conditions along the near horizontal propagation path described in Section 2.1, the Fried parameter

calculated by equation (50) will be $r_0 = 9.9\,cm$, while the Rytov variance for a plane wave $\sigma_I = 4.9$, obtained with the equation (58).

In Figure 28b) the time evolution of the digital combination of the received power for the six sub-apertures equipped with multimode fiber coupling ($P_2 - P_7$)can be observed (during one second), this combination is obtained by using the following expression:

$$\langle P_T \rangle(t) = \frac{1}{6}\sum_{i=2}^{7} P_i(t) \tag{71}$$

When performing this channel combination, the aperture averaging effect reduces the level of fluctuations, avoiding Deep fading of the received power.

With the expression (72) it is possible to obtain the normalized variance of the power detected by each of the apertures of the Multi Aperture Receiver:

$$\hat{\sigma}_i^2 = \frac{\langle P_i^2 \rangle - \langle P_i \rangle^2}{\langle P_i \rangle^2} \tag{72}$$

On the other hand, the covariance between two different channels is calculated, to verify how closely they are related to each other, as follows:

$$\hat{\sigma}_{ij}^2 = \frac{\langle (P_i - \langle P_i \rangle) \rangle \langle (P_j - \langle P_j \rangle) \rangle}{\langle P_i \rangle \langle P_j \rangle} \tag{73}$$

Where i and j represent each of the apertures, being able to take values $i, j = 2, \ldots 7$. Values between brackets $\langle \ldots \rangle$ denote the average value of the power obtained throughout the entire data series.

Table 2 shows the results when using the expression 73 to find the normalized covariance between all the channels of the multi aperture receiver. The values highlighted with gray, located on the diagonal of this table, are the normalized variances $\hat{\sigma}_i^2$, which have a bigger value than the rest of the quantities, which

show the normalized covariances $\hat{\sigma}_{ij}^2$ between the different optical sub-apertures. This means that, as expected, the relationship between channels is greater, the closer the sub-apertures are (neighboring sub-apertures), reaching their maximum in the case of each channel with itself. Note that the table is symmetrical around the diagonal, or $\hat{\sigma}_{ij}^2 = \hat{\sigma}_{ji}^2$.

The reduction in the variation of the fiber coupled optical power can be optimized by combining sub-apertures that are far from each other. For this, we calculate the sum of the power of different openings following the numbering described above:

$$\overline{P_N}(t) = \sum_{N}^{N+1} P_i(t) \tag{74}$$

Then the standard deviation of this data is calculated by:

$$\overline{\sigma_N} = \frac{1}{\langle \overline{P_N} \rangle} \sqrt{\langle \overline{P_N^2} \rangle - \langle \overline{P_N} \rangle} \tag{75}$$

Table 2. Normalized covariances $\hat{\sigma}_{ij}^2$ for different combinations of apertures.

i / *j*	***#2***	***#3***	***#4***	***#5***	***#6***	***#7***	
#2	0.28	0.16	0.18	0.08	0.07	0.08	
#3	0.16	0.28	0.06	0.04	0.07	0.16	
#4	0.18	0.06	0.28	0.16	0.08	0.04	
#5	0.08	0.04	0.16	0.26	0.14	0.05	
#6	0.07	0.07	0.084	0.14	0.25	0.14	
#7	0.08	0.16	0.04	0.05	0.14	0.22	

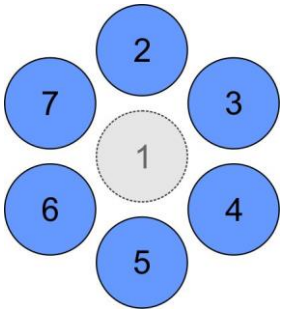

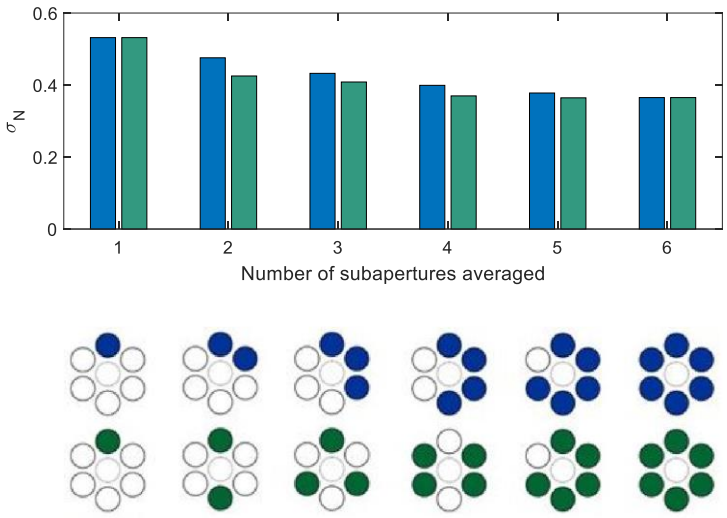

Figure 28. Reduction of the normalized standard deviation of the received power fluctuation, by increasing the average number of apertures for one turbulence condition $Cn^2 = 4.52\mathrm{e}^{-16}\ \left[\mathrm{m}^{-\frac{2}{3}}\right]$.

The results showed using bars in figure 28, are the result of combining sub-apertures for a case of atmospheric turbulence. The blue bars are obtained by averaging neighboring sub-apertures, while the green bars represent the result of combining distant openings. At the bottom of the figure 28 the sub-apertures used in each case can be seen schematically. Clearly, the smallest standard deviation of the data is reached when averaging distant sub-apertures.

At the same time, taking a larger series of points with different atmospheric turbulence conditions, the decrease in the normalized variance calculated with the expression 72, can be observed for different values of C_n^2. In blue, we can see the normalized variance of a single sub-apertures under different atmospheric conditions, while in red, we can see the result of averaging two of the openings, and finally, in green, the normalized variances obtained with digitally combination of the six sub-apertures available on the tiled optical receiver. This is shown in Figure 29.

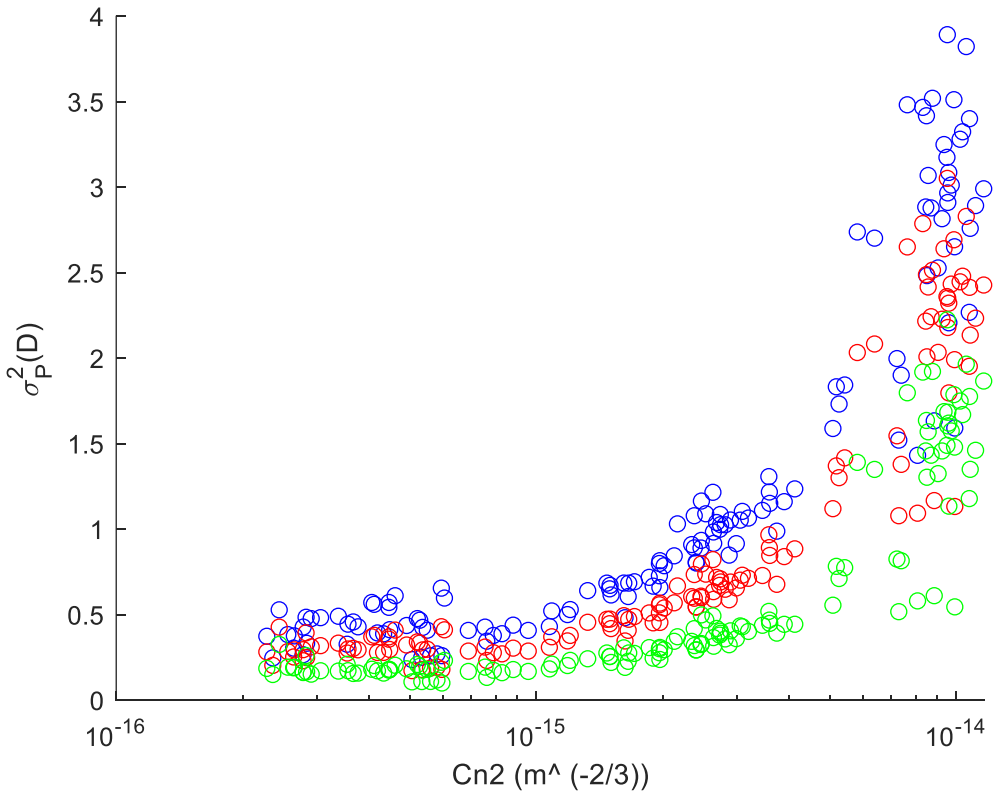

Figure 29. Reduction of the normalized standard deviation of the received power fluctuation, by increasing the average number of apertures for different turbulence conditions.

3.3. Digital versus optical combiners

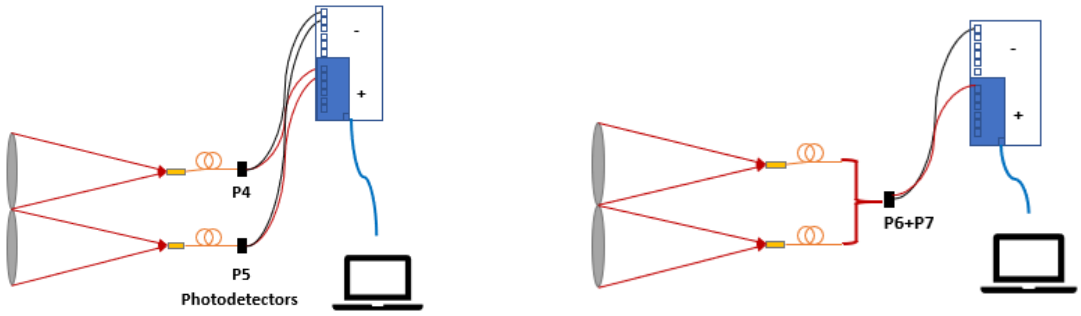

(a) (b)

Figure 30. Combination of 2 optical channels using a a) Digital fiber combiner and b) Optical Fiber combiner.

All the above combinations have been done digitally, after capturing each one separately, however, it is possible to use a fiber optic combiner to combine these channels and thus reduce the digital code necessary to average the power fluctuations received with the different channels of the multi aperture optical receiver. Therefore, it is worth comparing power fluctuations in both cases, to determine if the use of fiber combiners is feasible. It should be noted that the manufacturer of this fiber combiner offers an efficiency of $\eta \sim 50\%$, so it is expected that the average power of the received information will be considerably less when using fiber combiners. In order to observe the above combination methods, it is possible to observe Figure 30, It shows the process of obtaining data in both cases, for only two sub-apertures.

In the case of digital combiners, the optical power information obtained in each sub-aperture is transmitted to a multimode fiber that conducts the optical energy to a photodetector which sends a voltage signal to the digital analog converter, performing the necessary conversion for each channel, and with this, it is possible to obtain the temporary data tables of digitized optical power for each channel and perform the

corresponding average, this has the advantage that the information of each channel can be individually if an analysis of each particular opening is required.

On the other hand, in the case of the fiber combiner, the optical power information obtained by each opening is transmitted to its corresponding optical fiber, which in this case transmits the information to the fiber combiner, with a maximum capacity for 8 channels. This fiber combiner has a single channel output in which all the received and averaged information travels in an analogous way, this means that the combination and averaging speed is also much higher than in the case of the digital combiner (instantaneously), which reduces the time and computational capacity necessary to perform said combination digitally. Figure 31 shows the results of making such digital and optical combinations, for a value $Cn^2 = 7.808e^{-16}[m^{-\frac{2}{3}}]$ (week turbulence). In the black bars we can see the average optical power, represented by a voltage, obtained by combining two channels digitally and optically. The average power is lower in the case of the fiber combiner, due to the coupling efficiency of this element. On the other hand, the blue bars show the normalized variance, which has a very similar value in both cases. So, in the case of combining two sub-apertures, there is no advantage to doing it with optical combiners.

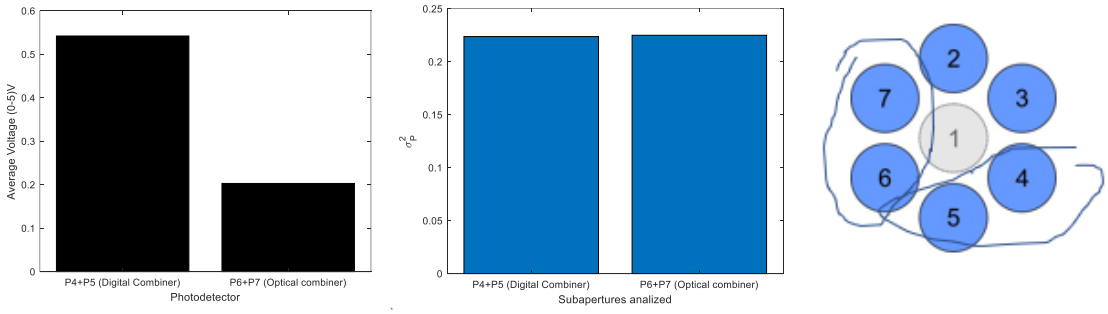

(a) (b) (c)

Figure 31. a) Average of the power fluctuations detected by two optical sub-apertures combined, using digital and optical combinations. b) Normalized variance of these two series. c) Sub-apertures used.

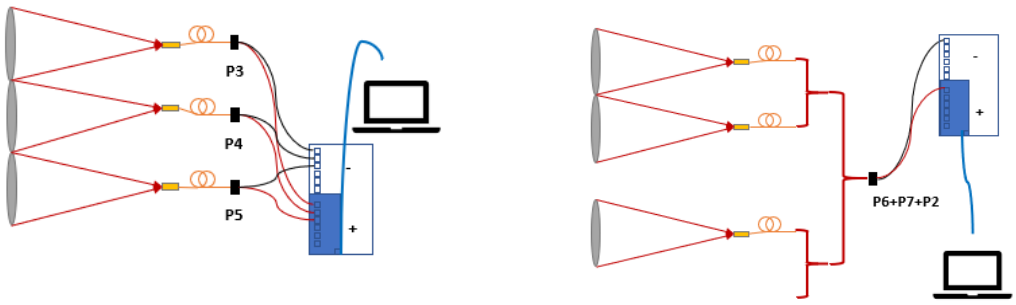

(a) (b)

Figure 32. Combination of 3 optical channels using a a) Digital fiber combiner and b) Optical Fiber combiner.

At the same time, it is possible to perform this combination for three different channels, in order to observe if these results change. The process of combining three optical channels is shown in Figure 32, in this case the atmospheric turbulence has a value of $Cn^2 = 2.714e^{-15}[m^{-\frac{2}{3}}]$ (weak turbulence). The results of this combination are shown in Figure 33. There is no advantage when performing optical combinations either, if we observe the normalized variance that has practically the same value in the case of both combinations. However, the average power value continues to decrease for the three-channel fiber combination.

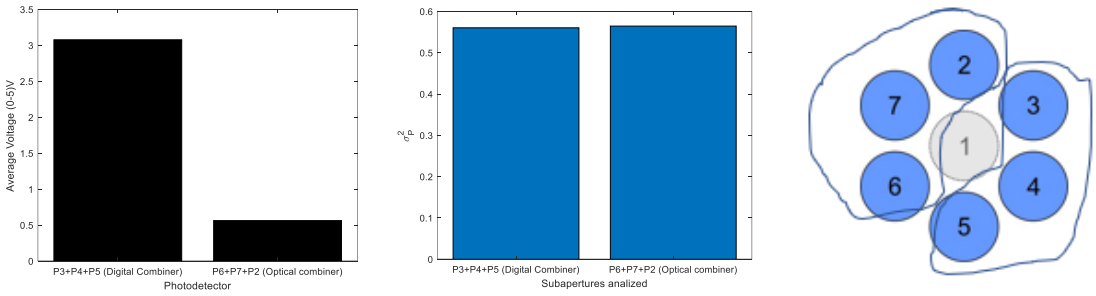

(a) (b) (c)

Figure 33. a) Average of the power fluctuations detected by three optical sub-apertures combined, using digital and optical combinations. b) Normalized variance of these two series. c) Sub-apertures used.

This is the maximum number of sub-apertures with which the optical and digital combinations can be compared, using the multi aperture receiver of six fiber-coupled channels, because if three channels are used for each case, the six corresponding channels will be occupied without leaving any channel available. However, it is possible to analyze four or more channels using a more sophisticated combination, in which all the channels are divided into two. One of these divisions goes directly to the fiber photodetector and the second goes to the fiber combiner. With this we can analyze optically combine all the channels, and at the same time obtain the information of each one digitally, to make the necessary comparisons. The combiner proposal for all sub-openings is shown in Figure 34.

It should be noted that, as mentioned above in the section 2.7 some microcontrollers have a limitation on the number of channels available, in addition to decreasing the sampling rate of said data, so, in the case of having a greater number of sub-apertures, it may be worth using fiber combiners, with the objective of obtaining a high speed in the acquisition of a large number of optical channels.

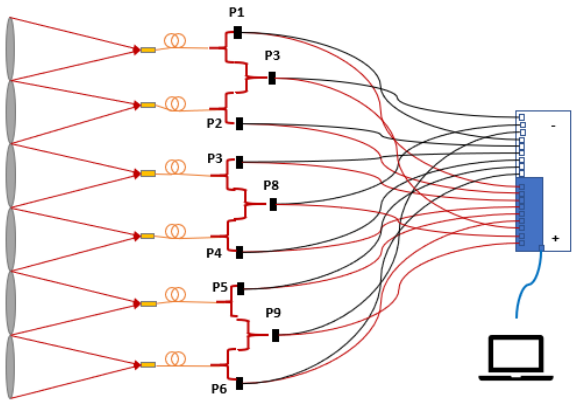

Figure 34. Combination method proposed to compare the combination of multiple sub-apertures.

3.4. Reducing the area of the monolithic receiver by applying masks in the image plane, in other to show the aperture averaging effect.

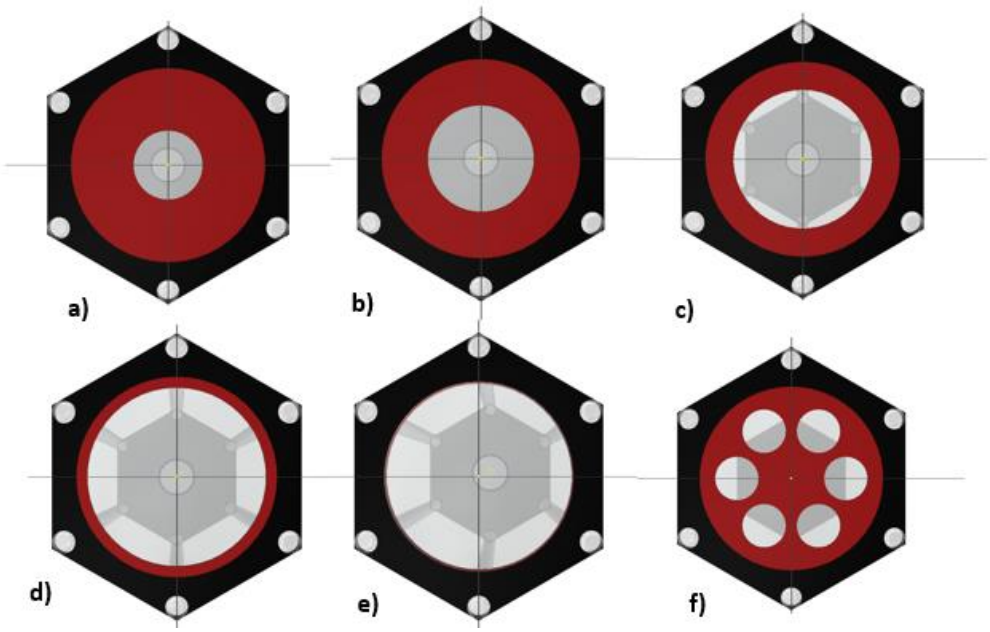

Figure 35. Increasing the collection area of a Monolithic Lens Receiver by using masks.

As mentioned in section 2.14, as an optical collector designed to detect fluctuations in optical power induced by atmospheric turbulence increases its collection diameter, it will decrease the normalized variance of the received power information, averaged over a period. This means that the larger the collection area, the smaller the power fluctuations received after a ha of light is propagated by atmospheric turbulence.

This experiment consists of reducing the area of the monolithic collector explained in Section 2.5, using masks with different diameters, which in turn corresponds to reducing the diameter of the entrance pupil of the telescope in question, this reduction of the diameter in question is illustrated The Figure 35.

The received optical power measurement will be performed for a time $t = 1\,minute$ for each mask, it is important that immediately after this minute, the mask is changed, losing as less time as possible between measurements, this because atmospheric turbulence can change quickly, and therefore the value offered by the scintillometer can also suddenly change. What is desired is that a similar atmospheric turbulence be preserved for all the masks used. Therefore, this experiment is designed in two processes: weak turbulence and strong turbulence.

- Weak turbulence:

To achieve these conditions of weak turbulence, it was necessary to perform optical power measurements at dusk, because at dusk the best atmospheric turbulence conditions are reached on a typical day, due to at these times of the day the atmospheric temperature is stable. The value of the constant C_n^2 had values of $1.891e^{-16} \leq C_n^2 \leq 2.160e^{-16}$ $[\mathrm{m}^{-\frac{2}{3}}]$. After performing the mask change process, we can obtain the bar graph observed in Figure 36, Where it can be observed that, by increasing the collection diameter of the telescope, the normalized variance of the received power also decreased, under conditions favorable weather conditions, practically 20%.

On the other hand, we can make other types of masks with a geometry that is not necessarily a perfect circle. In this case we analyze a mask that closely resembles the Multi Aperture Receiver seen from the front. This is a hexagonal arrangement of openings of $D = 3.3cm$, particularly the six openings on the periphery are taken, because these are the ones that incorporate a fiber optic coupling. This mask can be seen in Figure 35f).

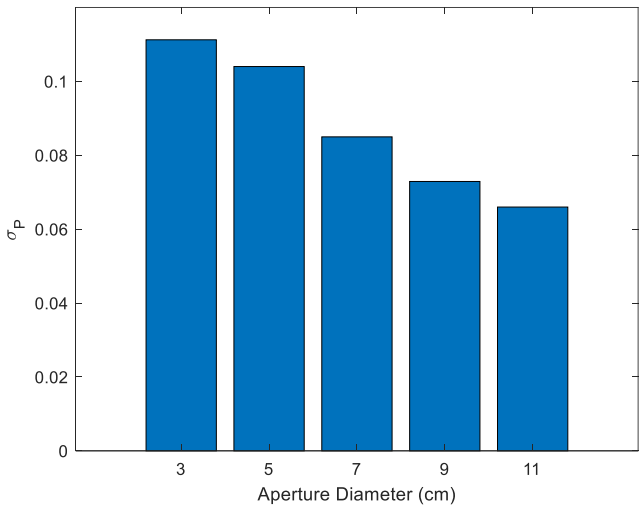

Figure 36. Reduction on the power fluctuations by increasing the diameter of a Monolithic Lens Receiver for weak atmospheric turbulence conditions.

One way to characterize the behavior of a Multi Aperture Receiver is to compare the received power fluctuations using a digital combination of the six peripheral optical channels and the power fluctuations using the mask described for the Monolithic Lens Receiver. In Figure 37, it can be observed that the fluctuations in optical power described with the normalized variance of the data remain very similar in the case of the Multi Aperture Receiver and the Monolithic Lens Receiver with the mentioned mask, this means that the MAR is a reliable instrument and that the increasing the number of sub-apertures used is precisely equivalent to increasing the collection area of a monolithic optical system.

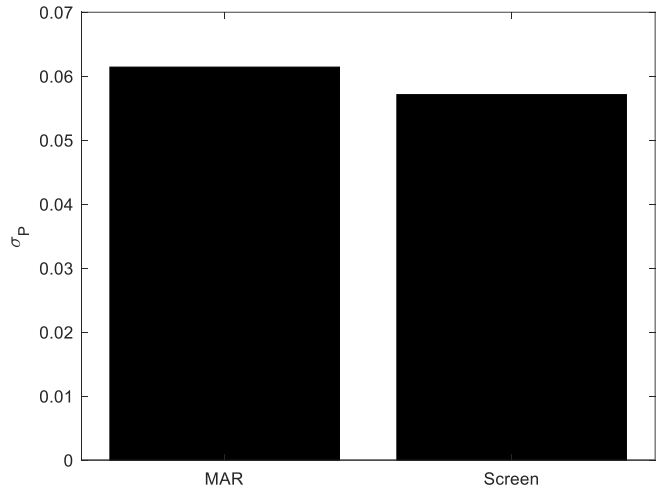

Figure 37. Multi Aperture Receiver vs. hexagonal mask (effective diameter), for weak turbulence conditions.

At this point, it is worth defining the effective diameter introduced in Section 2.5 for Multi Aperture Receivers, which will be a function of the collection diameter of each sub-aperture individually, this is obtained with a simple geometric analysis equating the total area of the sub-openings added with the area of an equivalent monolithic collector, then:

$$D_{eff} = \sqrt{n} D_{sub} \tag{76}$$

In the above expression D_{eff} represents the effective diameter of the equivalent monolithic collector, n is the number of sub-openings used and D_{sub} is the diameter of a single sub-opening. In this case $D_{sub} = 3.3\ cm$ and $n = 6$ so $D_{eff} = 8.08\ cm$.

- Strong turbulence.

To find the conditions of strong turbulence, the measurements must be made at solar noon, which is not necessarily the local noon, but rather is the time of day that is higher on the horizon and in solar radiation is the More powerful. At this time the air heats up causing greater atmospheric turbulence and a higher value of the constant Cn ^ 2, which in this case had values of $8.414e^{-15} \leq C_n^2 \leq 1.085e^{-14}$ $[m^{-\frac{2}{3}}]$. In this case also, the normalized variance decreases as the collection diameter increases, but in this case, the difference between the normalized variance using the larger diameter and the smaller diameter is more than 50%, so the stronger the is the atmospheric turbulence, the better the decrease in the normalized variance when increasing the collection area of the receiving optical instrument, this can be seen in Figure 38.

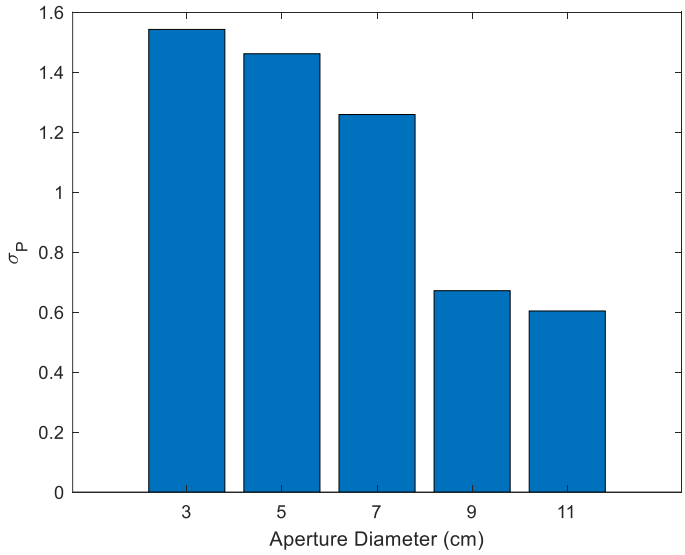

Figure 38. Reduction on the power fluctuations by increasing the diameter of a Monolithic Lens Receiver for strong atmospheric turbulence conditions.

In this case we can also implement the mask in Figure 35f) with $D_{eff} = 8.08\ cm$, to compare it with the digital combination of the six peripheral channels of the Multi Aperture Receiver, the normalized variances observed in this case are shown in Figure 37. A Although these normalized variances increase compared to the case with weak turbulence, it is possible to note that both have a very similar value again, so adding sub-openings is still completely analogous to increasing the effective collection diameter of a monolithic receiver, even in unfavorable weather conditions.

The demonstration that the effective collection diameter is reliable can be obtained if we compare the power fluctuations detected using the mask with a $D_{eff} = 8.08\ cm$, and those expected when using an aperture with this same diameter, in Figure 36 and 38, we can see these values using this approximation.

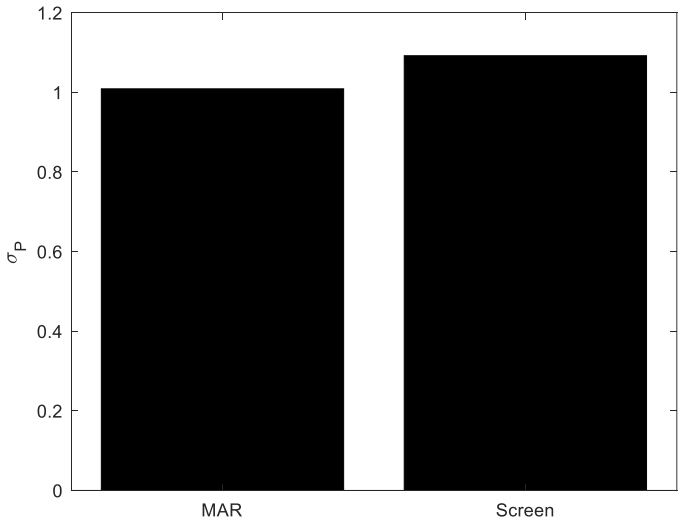

Figure 39. Multi Aperture Receiver vs. hexagonal mask (effective diameter), for strong turbulence conditions.

3.5. Wind speed determination using the cross-correlation function for a multi aperture receiver

The last experiment proposed in this work uses the normalized cross correlation function in order to determine the horizontal wind speed using a multi aperture receiver optical system, this method is currently used in commercial scintillometer, which have two detectors placed in line horizontally to capture wavefront distorted by atmospheric turbulence and their respective temporal functions of received optical power. Using the normalized time-lagged covariance function $C(\tau)$ (normalized correlation function) between these power functions, these scintillometers determine the speed of the transverse wind of the optical free-space path [59-61]. That normalized correlation function between two channels $\mathrm{P_i}(t)$ and $\mathrm{P_j}(t)$ is calculated as follows:

$$C(\tau) = \frac{\int_{t_1}^{t_2}[P_i(t+\tau) - \overline{P_i}][\mathrm{P_j}(t) - \overline{P_j}]dt}{\sqrt{\int_{t_1}^{t_2}[\mathrm{P_i}(t) - \overline{P_i}]^2\,dt \int_{t_1}^{t_2}[\mathrm{P_i}(t) - \overline{P_i}]^2\,dt}} \tag{77}$$

Where, $i, j = 1,2 \ldots 7$.

In this case, it is proposed to use this method using the sub-apertures of the tiled receiver system. To do this, the optical received power fluctuations through the six sub-apertures of this multi aperture receiver are captured for 10 seconds, this will generate a six-column table with the information of that detected power. The measurement was performed with a of $C_n^2 = 1.205e^{-15}[m^{-\frac{2}{3}}]$ (weak turbulence). Each column is a vector with the temporal variation in the optical power received by each sub-aperture. After obtaining these vectors, we take the normalized cross correlation function (77) between two channels to verify the temporal relationship between them. The upper channel $\mathrm{P}_2(t)$ is taken as a base vector, to compare it with the rest of the channels $\mathrm{P_j}(t)$. The lag in this case is $l = 0.02\ milliseconds$ (acquisition time between each measurement).

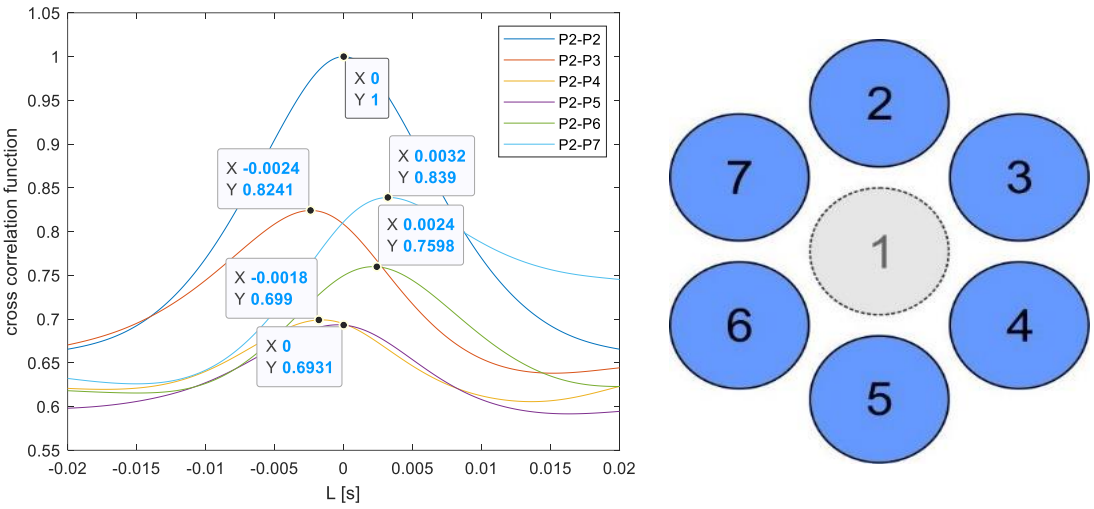

Figure 40. Normalized cross correlation function for the second sub-aperture with the rest of all.

Figure 38 shows the normalized cross correlation function of the channel $\mathrm{P}_2(t)$ with the rest of the channels during the first 20 milliseconds, as it can be seen, by applying this function to the vector $\mathrm{P}_5(t)$with itself, the auto normalized correlation function is obtained, that is why the maximum of this function has a unit value and is located at a lag equal to zero. On the other hand, it can be seen that the normalized correlation function has a peak at a lag equal to zero when comparing channel $\mathrm{P}_2(t)$ with channel $\mathrm{P}_2(t)$, which is curious because this is the lower channel of the multi aperture array, and it is also the farthest from the reference channel $\mathrm{P}_2(t)$, due to this distance, the value of the cross correlation function between these two channels is the lowest with respect to the comparison between the other channels. With the above, it can be ensured that there is a temporal relationship between the channels $\mathrm{P}_2(t)$ and $\mathrm{P}_5(t)$ maximum in a lag equal to zero, because the wind moves horizontally, moving the transmitted electromagnetic wave from the beacon platform laterally.

Following the previous logic we analyze the case of the cross correlation function between the central channel $\mathrm{P}_2(t)$ with the channels $\mathrm{P}_3(t)$ and $\mathrm{P}_4(t)$, channels that are on the right side of the multi aperture receiver, but have their value maximum of this function left on the graph of the cross correlation function, and practically at the same lag value. The same happens with the channels on the left of the multi aperture receiver, which have their maximum in the cross-correlation function with channel $\mathrm{P}_2(t)$ on the right side of the graph and practically also at the same lag value. This means that the relationship between the vertical channels is still present, denoting that the wind speed occurs horizontally.

Finally, taking the difference between the lags of the left channels with the right channels we can calculate the time in which these relationships take to have their maximum, finally, knowing the distance between these channels (0.064m), we can obtain the *effective wind speed* of the atmospheric channel during those 10 seconds of exposure, as follows:

$$W = \frac{d}{t} = \frac{d}{lag_1 - lag_2} = \frac{0.064}{0.003 + 0.0022} = \frac{0.064}{0.0052} = \ 12.30 \ [\frac{m}{s}] \tag{78}$$

The effective wind speed obtained in this case has a value of $W = 12.3\ [m\ /\ s]$. In Figure 38 shows the normalized cross correlation of the channel $P_2(t)$ with the rest of the channels during the first 20 milliseconds, as it can be seen, when we apply this function to the vector $P_2(t)$ with itself, we are obtaining the auto normalized correlation function, that is why the maximum of this function has a unit value and is located at a lag equal to zero. On the other hand, it can be seen that the normalized correlation function has a peak at a lag equal to zero when comparing channel $P_2(t)$ with channel $P_5(t)$, which is curious because this is the lower channel of the multi aperture array, and it is also the farthest from the reference channel $P_2(t)$, due to this distance, the value of the cross correlation function between these two channels is the lowest with respect to the comparison between the other channels. With the above, it can be ensured

that there is a temporal relationship between the channels $P_2(t)$ and $P_5(t)$ maximum in a lasg equal to zero, because the wind moves horizontally, carrying laterally, the transmitted electromagnetic wave from the beacon platform.

This method can approximately calculate the transverse speed of the wind as scintillometers currently do, using horizontally aligned detectors, however, as we can see in Figure 38, with the multi aperture receiver we can also obtain information on the temporal relationship of the vertical aligned channels of this system, which will enrich the information received, being able to measure vertical wind speeds if this is desired.

CHAPTER IV
SUMMARY CONCLUSION AND PATH FORWARD

In this work, the advantages of using a Multi Aperture Receiver have been studied in order to increase the collection area of an optical receiver, thereby decreasing by the effect of aperture averaging, the power fluctuations induced by a Gaussian beam propagating trough atmospheric turbulence.

The first chapter presents an introduction to the topic of free space optical communications, particularly, the effect of atmospheric turbulence, introducing the necessary concepts for a quantitative study of the relationship between the power fluctuations received by an optical system and the conditions of atmospheric turbulence. At the same time two phenomena present in optical receptors, caused by atmospheric turbulence have been described: the phenomenon of focal spot wander, and the effect of aperture averaging.

Moreover, the second chapter describes the experimental arrangement of the Intelligent Optics Laboratory at UD, used in this research project. In addition, the alignment process of a Multi Aperture Receiver is described.

With the first experiment we were able to observe that after the alignment of the sub-apertures of the Multi Aperture Receiver, the multimode fiber optic coupling ($\varnothing$=100μm) does not introduce extra optical power fluctuations to those detected directly with a photodetector ($\varnothing$=2.2mm), however, as the diameter of that photodetector increases, the sample rate of the sensor is decreased , so many of the optical power fluctuations will not be detected, particularly in the case of strong atmospheric turbulence. Therefore, this

experiment has been able to verify the effectiveness of the multimode fiber coupling and the importance of size of the optical sensor used.

The second experiment describes the reduction of scintillation by increasing the number of sub-apertures used in a Multi Aperture Receiver system. In this section, the concept of "sub apertures averaging" has been defined by its similarity to the averaging aperture phenomenon valid for monolithic receivers. On the other hand, it has been shown that, by using neighboring openings, there is a lower reduction in power fluctuations, comparing them with the results obtained by combining the received power into opposite sub-apertures, i.e. the normalized variance is always lower in the case of combining opposite apertures. In this same experiment the covariance function has been used to determine the relationship between the information received by each channel with respect to another, here it has been possible to determine that the farther the sub-openings, the less related they will be. Because these measurements were performed for different atmospheric turbulence conditions, it is possible to perform a direct comparison between the C_n^2 factor and the normalized variance of the optical power received, which represents an opportunity to develop Scintillometer based on Multi Aperture Receiver systems.

The combination of the optical power received by each sub-aperture was performed digitally, however, in the third experiment it was possible to compare that, by using optical combiners based on fiber dividers, the normalized variance of this power is not increased, so that optical combination does not increase the scintillation. However, the average power is drastically reduced due to the coupling efficiency of the fiber combiners.

With the fourth experiment, the phenomenon of aperture averaging has been tested, reducing the scintillation effect by increasing the diameter of a Monolithic Lens Receiver. In addition,

an effective diameter has been defined for Multi Aperture Receivers, with the aim of comparing the phenomenon of sub apertures averaging with the well-known effect of aperture averaging.

The latest experiment explored the possibility of using a Multi Aperture Receiver as a transverse wind speed meter in an atmospheric channel, using the normalized correlation function between the horizontal opposite channels of this optical system.

With all the above experiments, the effectiveness of Multi Aperture Receiver systems to reduce the scintillation phenomenon for free space optical communication systems, is showed. This effectiveness, in addition to the advantages of manufacturing and implementation, we can ensure that the best way to increase the area of optical systems is by adding sub-apertures in different geometrical arrangements.

As future activities in this research work, the use of an adaptive optics system could be implemented to further reduce the optical power variations received. In addition, it will also be necessary to change the multimode optical fibers used by single mode fibers, which have a much larger bandwidth, but a much smaller core diameter.

BIBLIOGRAPHY

[1] Andrews, L. C., & Phillips, R. L. (2005). Laser beam propagation through random media. SPIE.9].

[2] V. I. Tatarskii. (1975). The Effects of the Turbulence Atmosphere on Wave Propagation. Jerusalem: Israel Program for Scientific Translations.

[3] Wallace, J. M., & Hobbs, P. V. (2006). *Atmospheric science: an introductory survey* (Vol. 92). Elsevier.

[4] Bolin, B., & Doos, B. R. (1989). Greenhouse effect.

[5] U.S. Standard Atmosphere. (1976), U.S. Government Printing Office, Washington, D.C.

[6] Clifford, S. F. (1978). The classical theory of wave propagation in a turbulent medium. In Laser beam propagation in the atmosphere (pp. 9-43). Springer, Berlin, Heidelberg.

[7] J.C.Owens. (1967) Appl. Opt. 6, 51

[8] M.L.Wesely, E.C. Alcaraz. (1973) J. Geophys. Res. 78, 6224

[9] C.A.Friehe, J.C.LaRue, F.H.Champagne, C.H.Gibson, C.F.Dreyer. (1975) J. Opt. Soc. Am. 65, 1502.

[10] Yaglom, A. M. (1981). Laws of small-scale turbulence in atmosphere and ocean (in commemoration of the 40th anniversary of the theory of locally isotropic turbulence). Izv. Acad. Sci. USSR Atmos. Oceanic Phys., 17, 919–935.

[11] Kolmogorov, A. N. (1962). A refinement of previous hypotheses concerning the local structure of turbulence in a viscous incompressible fluid at high Reynolds number. J. Fluid Mech., 13(1), 82–85.

[12] Azoulay, E., Thiermann, V., Jetter, A., Kohnle, A., and Azar, Z. (1988). Optical measurement of the inner scale of turbulence. J. Phys. D: Appl. Phys., 21(10S), S41–S44.

[13] Hardy, J. W. (1998). Adaptive Optics for Astronomical Telescopes. Oxford University Press, New York.

[14] Gurvich, A. S., Kon, A. I., Mironov, V. L., and Khmelevtsov, S. S. (1976). Laser Radiation in a Turbulent Atmosphere. Nauka, Moscow.

[15] Gracheva, M. E. and Gurvich, A. S. (1980). Simple models of turbulence. Izv. Akad. Nauk SSSR, Fiz. Atm. Okeana, 16(10), 1107–1111.

[16] Hufnagel, R. E. (1974). Variations of atmospheric turbulence. In Digest of Topical Meeting on Optical Propagation through Turbulence,Washington, D.C., pp.WA1–1–WA1–4. Optical Society of America.

[17] Valley, G. C. (1980). Isoplanatic degradation of tilt correction and short-term imaging systems. Appl. Optics, 19(4), 574–577.

[18] M. S. Scholl, G. N. Lawrence, “Diffraction modeling of a space relay experiment,” Opt. Eng., **29**(3), 271-278 (1990). https://doi.org/10.1117/12.55581

[19] Tatarskii, V. I. (1961). Wave Propagation in a Turbulent Medium. McGraw-Hill Series in Electrical Engineering. McGraw-Hill, New York.

[20] Hill, R. J. and Clifford, S. F. (1978). Modified spectrum of atmospheric temperature fluctuations and its application to optical propagation. J. Opt. Soc. Am., 68(7), 892–899.

[21] Andrews, L. C. (1992). An analytical model for the refractive index power spectrum and its application to optical scintillations in the atmosphere. J. Mod. Opt., 39(9), 1849–1853.

[22] Maxwell, J. C. (1890). The Scientific Papers of James Clerk Maxwell.. (Vol. 2). University Press.

[23] Korotkova, O., Salem, M., & Wolf, E. (2004). The far-zone behavior of the degree of polarization of electromagnetic beams propagating through atmospheric turbulence. Optics Communications, 233(4-6), 225-230.

[24] Yang, P., Bi, L., Baum, B. A., Liou, K. N., Kattawar, G. W., Mishchenko, M. I., & Cole, B. (2013). Spectrally consistent scattering, absorption, and polarization properties of atmospheric ice crystals at wavelengths from 0.2 to 100 μ m. Journal of the Atmospheric Sciences, 70(1), 330-347.

[25] Pal, S. R., & Carswell, A. I. (1985). Polarization anisotropy in lidar multiple scattering from atmospheric clouds. Applied optics, 24(21), 3464-3471.

[26] Rytov, S. M., Kravtsov Yu, A., & Tatarskii, V. I. (1989). Wave Propagation through Random Media (Principles of Statistical Radiophysics vol 4).

[27] Ricklin, J. C., & Davidson, F. M. (2002). Atmospheric turbulence effects on a partially coherent Gaussian beam: implications for free-space laser communication. JOSA A, 19(9), 1794-1802.

[28] Poon, T. C., & Banerjee, P. P. (2001). Contemporary optical image processing with MATLAB. Elsevier.

[29] LMiller, W. B., Ricklin, J. C., & Andrews, L. C. (1993). Log-amplitude variance and wave structure function: a new perspective for Gaussian beams. JOSA A, 10(4), 661-672.

[30] Gbur, G., & Wolf, E. (2001). The Rayleigh range of Gaussian Schell-model beams. journal of modern optics, 48(11), 1735-174.

[31] Nelson, W., Palastro, J. P., Davis, C. C., & Sprangle, P. (2014). Propagation of Bessel and Airy beams through atmospheric turbulence. JOSA A, 31(3), 603-609.

[32] Gu, Y., & Gbur, G. (2010). Scintillation of pseudo-Bessel correlated beams in atmospheric turbulence. JOSA A, 27(12), 2621-2629.

[33] Cox, M. A., Mphuthi, N., Nape, I., Mashaba, N. P., Cheng, L., & Forbes, A. (2020). Structured Light in Turbulence. arXiv preprint arXiv:2005.14586.

[34] Ishimaru, A. (1978). *Wave Propagation and Scattering in Random Media*. Academic Press, New York.

[35] Tatarskii, V. I. (1961). Wave Propagation in a Turbulent Medium. McGraw-Hill Series in Electrical Engineering. McGraw-Hill, New York.

[36] Fried, D. L. (1966). Optical resolution through a randomly inhomogeneous medium for very long and very short exposures. JOSA, 56(10), 1372-1379.

[37] Brown, W. P. (1966). Validity of the Rytov approximation in optical propagation calculations. JOSA, 56(8), 1045-1052.

[38] Andrews, L. C., Phillips, R. L., & Weeks, A. R. (1997). Rytov approximation of the irradiance covariance and variance of a retroreflected optical beam in atmospheric turbulence. JOSA A, 14(8), 1938-1948.

[39] Mikesell, A. H., Hoag, A. A., & Hall, J. S. (1951). The scintillation of starlight. JOSA, 41(10), 689-695.

[40] Andrews, L. C. (1992). Aperture-averaging factor for optical scintillations of plane and spherical waves in the atmosphere. JOSA A, 9(4), 597-600.

[41] Lutomirski, R. F., & Yura, H. T. (1969). Aperture-averaging factor of a fluctuating light signal. JOSA, 59(9), 1247-1248.

[42] Fried, D. L. (1967). Aperture averaging of scintillation. JOSA, 57(2), 169-175.

[43] Kon, A. I. (1969). Averaging of spherical-wave fluctuations over a receiving aperture. Radiophysics and Quantum Electronics, 12(1), 122-124.

[44] Churnside, J. H. (1991). Aperture averaging of optical scintillations in the turbulent atmosphere. Applied Optics, 30(15), 1982-1994.

[45] M. Valero, M. Strojnik, I. Salgado-Tránsito, "Design, manufacturing and testing of a CPV + T based on a Cassegrain: trough configuration," Proc. SPIE 11128, Infrared Remote Sensing and Instrumentation XXVII, 111280Z (9 September 2019); https://doi.org/10.1117/12.2527482

[46] Malacara, D. (2015). Óptica básica. Fondo de cultura económica.

[47] Ricklin, J. C., Davidson, F. M., & Weyrauch, T. (2002, January). Free-space laser communication using a partially coherent laser source. In Optics in Atmospheric Propagation and Adaptive Systems IV (Vol. 4538, pp. 13-23). International Society for Optics and Photonics.

[48] Strojnik, M., & Scholl, M. K. (2014). Extrasolar planet observatory on the far side of the Moon. Journal of Applied Remote Sensing, 8(1), 084982.

[49] Cerecedo, L. O. L., Pitalua-Diaz, N., Transito, I. S., Contreras, L. E. V., & Bulnes, C. A. (2013, November). Optical performance modeling of a solar tower heliostat field and estimation of receiver temperature. In 2013 IEEE International Autumn Meeting on Power Electronics and Computing (ROPEC) (pp. 1-6). IEEE.

[50] Akiyama, K., Alberdi, A., Alef, W., Asada, K., Azulay, R., Baczko, A. K., ... & Blackburn, L. (2019). First M87 event horizon telescope results. IV. Imaging the central supermassive black hole. The Astrophysical Journal Letters, 875(1), L4.

[51] J. Hartmann (1900), “Bemerkungen uber den Bau und die Justirung von Spektrograpen,” Zt. Instrumentenkd. 20, 47–58.

[52] Malacara-Hernández, D., & Malacara-Doblado, D. (2015). What is a Hartmann test? Applied optics, 54(9), 2296-2301.

[53] B. C. Platt and R. V. Shack (1971), “Lenticular Hartmann screen,” Opt. Sci. Newsl. 5, 15–16.

[54] Vorontsov, M. A., Weyrauch, T., Beresnev, L. A., Carhart, G. W., Liu, L., & Aschenbach, K. (2009). Adaptive array of phase-locked fiber collimators: analysis and experimental demonstration. IEEE Journal of Selected Topics in Quantum Electronics, 15(2), 269-280.

[55] Vorontsov, M. A. (2020). U.S. Patent Application No. 16/778,562.

[56] Liu, L., & Vorontsov, M. A. (2005, August). Phase-locking of tiled fiber array using SPGD feedback controller. In Target-in-the-Loop: Atmospheric Tracking, Imaging, and Compensation II (Vol. 5895, p. 58950P). International Society for Optics and Photonics.

[57] Malacara, D. (Ed.). (2007). Optical shop testing (Vol. 59). John Wiley & Sons.

[58] Vaidyanathan, P. P. (2001). Generalizations of the sampling theorem: Seven decades after Nyquist. IEEE Transactions on Circuits and Systems I: Fundamental Theory and Applications, 48(9), 1094-1109.

[59] Poggio, L. P., M. Furger, A. H. Prévôt, W. K. Graber, and E. L. Andreas, (2000): Scintillometer Wind Measurements over Complex Terrain. J. Atmos. Oceanic Technol., 17, 17–26.

[60] Andreas, E. L, (1991): Using scintillation at two wavelengths to measure path-averaged heat fluxes in free convection. Bound. -Layer Meteor., 54, 167–182.

[61] Biltoft, C. A., (1989): Field testing of a crosswind scintillometer. Proc. SPIE, 1115, 167–178.